Australian Government
Department of Defence
Defence Science and
Technology Organisation

Application of the Fractional Fourier Transform and S-Method in Doppler Radar Tomography

H.T. Tran and R. Melino

Electronic Warfare and Radar Division

Defence Science and Technology Organisation

DSTO–RR–0357

ABSTRACT

Doppler radar tomography is a technique which uses only the Doppler profiles of a rotating target as projections in two-dimensional radar tomography to obtain an image of the target. The work demonstrates, for the first time, the application of the fractional Fourier transform and the S-Method in improving the image resolution. The performance is shown to be significantly better than that available with traditional Fourier transform-based methods.

Published by

DSTO Defence Science and Technology Organisation
PO Box 1500
Edinburgh, South Australia 5111, Australia

Telephone: 08 7389 5555
Facsimile: 08 7389 6567

AR No. 014–825
August, 2010

APPROVED FOR PUBLIC RELEASE

Application of the Fractional Fourier Transform and S-Method in Doppler Radar Tomography

Executive Summary

Radar tomography is the process of constructing a two-dimensional image from one-dimensional projections obtained from radar returns. The backscatter from radar provides Doppler information of the scatterer giving the frequency characteristics over time, or in the case of rotating objects, over varying aspect angle. These frequency domain projections are used for Doppler radar tomographic imaging.

Doppler radar tomography, in conjunction with other signal processing techniques, can also be used to estimate the physical parameters of a rotating object. For helicopter targets, the characteristics of the rotor blades (blade length, number of blades and rotation rate) and rotor hub features, can be used as discriminates for automatic target recognition. The ability to accurately estimate these features effects the ability to correctly classify targets quickly and is directly related to the frequency resolution of the system.

The resolution of a tomographic image depends on the resolution of the input projections. Here, we strive for high frequency resolution so that closely spaced scatterers can be resolved and hence appear in the tomographic image. However, the long coherent processing interval needed to increase frequency resolution introduces a frequency spread (chirp) for each scatterer (due to the scatterer motion), giving 'smeared' projections and hence smeared images.

The fractional Fourier transform is a technique that can be used to identify chirps in a signal so that they can be spectrally compressed using the S-Method. The result is high resolution projections, without the frequency spread, and a clear and sharp tomographic image. Long integration times allow closely spaced scatterers to be easily resolvable and performance is improved in the presence of noise when compared to the traditional Fourier transform-based method, which is confined to short coherent processing intervals.

This report successfully demonstrates the application of the fractional Fourier transform and the S-Method techniques on simulated rotating point scatterers and real helicopter data. The improved resolution of the projections and clarity of tomographic images makes identifying the position of scatterers easier and, for the case of real helicopter data, the blade tip positions more discernible.

The accurate estimation of target parameters using high resolution imaging, is expected to improve automatic target recognition performance and can be used on a variety of targets such as helicopter rotor blades, propellers on propeller driven aircraft or slower rotating objects such as rotating antenna structures on ships.

Authors

Dr. Hai-Tan Tran
Electronic Warfare and Radar Division

Hai-Tan Tran graduated from the University of Sydney in 1990 and obtained his PhD degree from the Australian National University in Canberra in 1993, in the field of nonlinear guided-wave optics. He spent the next three years as a postdoctoral research fellow in the Mathematics Department of the Australian Defence Force Academy, also in Canberra, working on the theory and simulation of spatial optical solitons in dielectric media, before joining the Electronic Warfare and Radar Division of DSTO, Edinburgh, in 1996. His current research interests include radar automatic target recognition, radar electronic protection, and various topics in signal processing.

Mr. Rocco Melino
Electronic Warfare and Radar Division

Rocco Melino works for the Electronic Warfare and Radar Division of DSTO in the field of radar automatic target recognition and radar system modelling and analysis. He has a Bachelor Degree in Engineering from the University of South Australia and a Masters Degree in Signal and Information Processing from the University of Adelaide.

Contents

Figures

Tables

Glossary

CAT - Computer Aided Tomography

CPI - Coherent Processing Interval

CW - Continuous Wave

FFT - Fast Fourier Transform

FrFT - Fractional Fourier Transform

FT - Fourier Transform

ISAR - Inverse Synthetic Aperture Radar

LFM - Linear Frequency Modulation

PRF - Pulse Repetition Frequency

PSF - Point Spread Function

RPM - Revolutions Per Minute

STFT - Short Time Fourier Transform

TFDS - Time-frequency Distribution Series

WVD - Wigner-Ville Distribution

1 Introduction

Tomography is a mathematical technique of reconstructing a 2-dimensional function from 1-dimensional projections of the function at different aspect angles. This involves the Radon transform, first described by Johann Radon [1], and back-projection algorithms to reconstruct the original function. It can also be described as a method of computing the inverse 2-dimensional Fourier transform using a collection of 1-dimensional projections which can be measured directly from an object of interest. In X-ray tomography, which is usually referred to as Computer Aided Tomography (CAT), the projections are density measurements. In radar tomography, they are range profiles.

For radars of high bandwidth, the range profiles can be down-range profiles which are basically 1-dimensional images of a target in the down-range dimension. For narrow-band radars, the range profiles are necessarily cross-range profiles which can be obtained through coherent Doppler processing, which means the dwell time requirement for narrow-band must be greater than in the case of wide-band radars. The trade-off between bandwidth and time is a manifestation of the well-known and fundamental *time-bandwidth product* which has a significant role in setting the performance limits of any radar system.

The theory of tomography itself has been well described by many authors, such as in [2]. Our present work is focused on the use of Doppler tomography in narrow-band radars and applying time-frequency processing techniques to achieve high-resolution images of rotating targets. D. Mensa [3] was among the first authors to have used the term 'Doppler tomography'. Mensa described the basic ideas of Doppler tomography: all scattering centres at the same cross range of an illuminated rigid target impart the same Doppler frequency components in the returned signal, and hence a Doppler profile can be used to represent a cross-range profile. As the target rotates, a continuum of such projections can then be obtained and inverted by tomography to produce an image. G. Fliss [4] later applied the idea to the imaging problem of helicopter rotor blades and hubs, using a simple single frequency continuous-wave (CW) instrumentation radar. Fliss demonstrated that it is possible, using Doppler tomography, to image the tips of the blades which are the main scattering centers of the blade rotors.

Resolution of a Doppler tomographic image directly depends on the resolution of the projections used in the tomographic processing. As a target rotates, the instantaneous cross range position of a rotating scattering point, relative to the center of rotation, defines its instantaneous Doppler frequency, while the finite coherent processing interval (CPI) required to produce a projection undesirably introduces a finite frequency spread for each point scatterer. In other words, each point scatterer in a projection is represented by a chirped signal of finite spectral extent, rather than a 'pure tone', causing a smearing in a projection, which in turn leads to a degradation of the tomographic image, if not appropriately processed. The longer the CPI, the finer the Doppler filter width would become, but the smearing due to cross-range motion also gets worse.

Known techniques for spectral compression for chirped signals include bilinear techniques such as the Wigner-Ville Distribution (WVD), the Cohen's class, and the time-frequency distribution series (TFDS) as discussed in V. Chen's book [5]. The spectral compression performance of the WVD is excellent except for the existence of cross terms. A recently proposed variant of the WVD is the S-Method [6], which could remove the cross

terms while also substantially reducing the computational cost. Unfortunately, when the instantaneous component frequencies are closely spaced, cross terms are still unavoidable; and this is indeed the case in Doppler tomography. Scattering centers may line up with the radar line of sight, causing spectral overlapping and crossing of the chirp components.

Fortunately, the recently developed technique of fractional Fourier transform (FrFT) has become available, which can turn the spread-out spectrum of a chirp signal into a well-compressed spike in the 'fractional frequency' domain. We have exploited the useful property of the FrFT and, in combination with the use of the S-Method, developed an algorithm for extracting and spectrally compressing multiple chirp signals, to produce clean and sharpened projections for tomographic processing. The application of the FrFT to Doppler tomography and the new algorithm of extracting and compressing multiple chirp signals are the main contribution of this work, which are demonstrated using both simulated and real data.

An outline of the Report is as follows. Section 2 gives an overview of the theory of 2D tomography in general and the system requirements for Doppler tomography in particular. Section 3 briefly describes the fractional Fourier transform and its applicability to Doppler tomography. Section 4 describes the S-Method and why it is useful for the current problem. Section 5 presents the algorithm of multiple chirp extraction and compression. Section 6 describes and discusses the results when applied to both simulated and real data. The final Section contains the concluding remarks.

2 An Overview of 2D Radar Tomography

This section summarises the theory of two-dimensional tomographic imaging, explains what is meant by 'Doppler radar tomography', and finally discusses resolution and system requirement issues when the projections used in the tomographic processing are based on the traditional Fourier transform.

2.1 The Basic Theory

The essence of tomographic imaging is the Back-Projection Algorithm [2, 7, 8, 9, 10], which can be formulated as a general 2D Fourier analysis technique as follows. For a 2D real-valued function $q(x, y)$, as shown in Figure 1, the projection $p_\theta(r)$ along a line through the origin at angle θ, which is also called the Radon Transform, can be defined as

$$p_\theta(r) = \int_{-\infty}^{\infty} \int_{-\infty}^{\infty} q(x, y)\, \delta(x \cos\theta + y \sin\theta - r)\, dx\, dy. \tag{1}$$

The spatial Fourier transform $P_\theta(f_r)$ of $p_\theta(r)$, with spatial frequency in the r- dimension denoted as f_r, is

$$\begin{aligned} P_\theta(f_r) &= \int_{r=-\infty}^{\infty} p_\theta(r)\, e^{-i2\pi f_r\, r}\, dr & (2)\\ &= \int_{-\infty}^{\infty} \int_{-\infty}^{\infty} q(x, y)\, e^{-i2\pi(f_x\, x + f_y\, y)}\, dx\, dy & (3)\\ &= Q_\theta(f_x, f_y), & (4) \end{aligned}$$

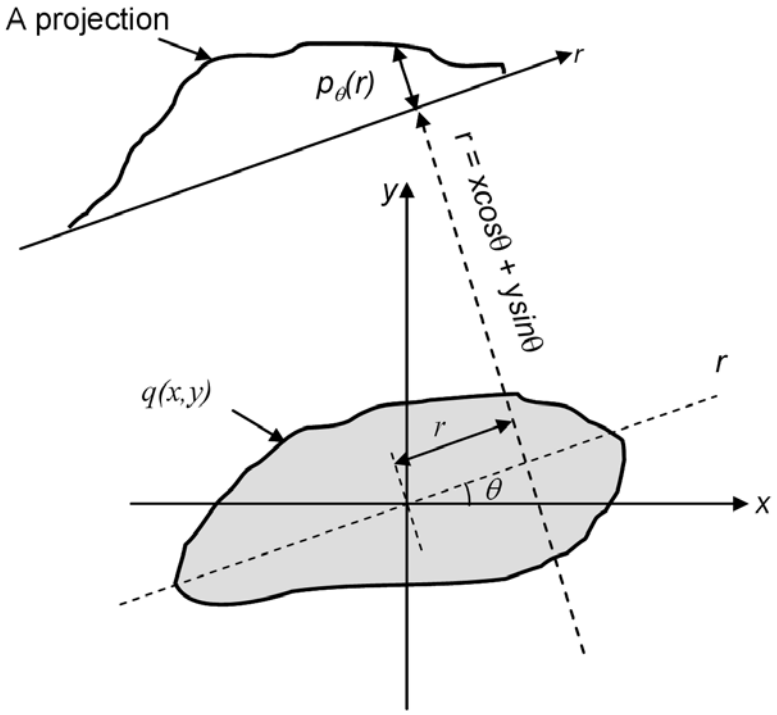

Figure 1: *Projection of a 2D function,* $q(x, y)$.

upon the substitution of (1). Here,

$$f_x = f_r \cos\theta, \quad f_y = f_r \sin\theta$$

are the spatial frequency components in the x- and y- dimensions along the slice at angle θ, and $Q_\theta(f_x, f_y)$ is the 2D Fourier transform of $q(x, y)$ along this direction, i.e. a slice of $Q_\theta(f_x, f_y)$. The spatial frequency f_r is related to the temporal frequency f through $f_r = 2f/c$. The Fourier transform of a projection of a two-dimensional function is thus a slice of the 2D Fourier transform of that function. This is the so-called *Projection-Slice Theorem.*

Once $Q_\theta(f_x, f_y)$ is constructed from many such slices at a range of aspect angle θ, $q(x, y)$ can be obtained from the inverse 2D transform. However, noting that $df_x\, df_y = f_r\, df_r\, d\theta$, the inverse 2D transform can be done on $Q_\theta(f_r)$ in polar coordinates, as follows:

$$\begin{aligned}
q(x,y) &= \int_{-\infty}^{\infty}\int_{-\infty}^{\infty} Q_\theta(f_x, f_y)\, e^{i2\pi(x\, f_x + y\, f_y)}\, df_x\, df_y && (5)\\
&= \int_0^{2\pi}\int_0^{\infty} Q_\theta(f_r)\, e^{i2\pi f_r(x\cos\theta + y\sin\theta)}\, f_r\, df_r\, d\theta && (6)\\
&= \int_0^{\pi}\left[\int_{-\infty}^{\infty} |f_r| P_\theta(f_r)\, e^{i2\pi f_r(x\cos\theta + y\sin\theta)}\, df_r\right] d\theta && (7)\\
&= \int_0^{\pi} \mathcal{F}^{-1}\left\{|f_r|\, P_\theta(f_r)\right\}_{(x\cos\theta + y\sin\theta)}\, d\theta, && (8)\\
&= \int_0^{\pi} \mathcal{F}^{-1}\left\{\mathrm{sgn}(f_r)\, f_r\, P_\theta(f_r)\right\}_{(x\cos\theta + y\sin\theta)}\, d\theta. && (9)
\end{aligned}$$

The subscript $(x\cos\theta + y\sin\theta)$ means the inverse Fourier transform (FT), denoted by $(\mathcal{F}^{-1})$, is calculated at $r = x\cos\theta + y\sin\theta$. This $\mathcal{F}^{-1}$ operation is where most of the complexity of implementation of the above result lies.

There are two known approaches to calculate the above integral [2]. The first approach, called the Filter Back-Projection method, calculates in the inverse FT in (8) directly (and numerically). The second approach, called the Convolution Back-Projection method, applies the convolution theorem to the inverse FT in (9). In general, if $p(x)$ is any real-valued bounded function, then

$$\mathcal{F}\left\{\frac{d\,p(x)}{dx}\right\} = \int_{-\infty}^{\infty} \frac{d\,p(x)}{dx}\, e^{-i2\pi fx}\, dx = i2\pi f\, P(f).$$

From theory on Hilbert transform,

$$\mathcal{F}^{-1}\left\{\mathrm{sgn}(f)\right\} = h(x) = -\frac{1}{i\pi x},$$

then the convolution theorem leads to [2]

$$\begin{aligned}
\mathcal{F}^{-1}\left\{\mathrm{sgn}(f_r)\, f_r\, P_\theta(f_r)\right\}_{(x\cos\theta+y\sin\theta)} &= \frac{1}{i2\pi}\left\{h(r)\otimes\frac{d\,p_\theta(r)}{dr}\right\}_{r=x\cos\theta+y\sin\theta} && (10)\\
&= \frac{1}{2\pi^2}\left\{\frac{1}{r}\otimes\frac{d\,p_\theta(r)}{dr}\right\}_{r=x\cos\theta+y\sin\theta} && (11)\\
&= \frac{1}{2\pi^2}\int \frac{1}{x\cos\theta + y\sin\theta - t}\,\frac{d\,p_\theta(t)}{dt}\,dt && (12)
\end{aligned}$$

What remains is to integrate this distribution (or grid) in the (x, y) plane over a range of angles θ between 0 and π. In our work, we have used the Filter Back-Projection method.

2.2 Doppler Radar Tomography

In applications, the projection $p_\theta(r)$ in the basic theory described above, can be obtained in at least two different forms. It may be in the form of a *range profile* of a rotating target from radar with a high sampling rate, which may be the case for radars with an ISAR capability. Alternatively, it may be in the form of a Doppler profile of a rotating target, which can be obtained by a narrow-band Doppler radar.

The technique of radar tomography which uses the Doppler profiles of a rotating target as projections may be called 'Doppler radar tomography' and is the main subject matter of the present report.

As a rigid object rotates about an origin such as that depicted in Figure 1, all points at constant cross-range (in the x dimension) offset from the origin will have the same Doppler shift, assuming the receiving antenna is located in the negative y direction. This means that the magnitude spectrum of the Fourier transform of a sufficiently long segment of samples can be interpreted as a cross-range projection of the object. In other words, if

$s(t;t_k)$; $t_k < t < t_k + T_{CPI}$ denotes the received time signal for one CPI with the corresponding averaged angle θ_k (say), and if $S(f,t_k)$ denotes its short-time Fourier spectrum at slow time t_k,

$$S(f,t_k) = \int_{t_k}^{t_k+T_{CPI}} w(t-t_k)\, s(t,t_k)\, e^{-i2\pi ft}\, dt, \tag{13}$$

then a cross-range projection $p_{\theta_k}(r)$ can be obtained as

$$p_{\theta_k}(r) = |S(f,t_k)|\,, \tag{14}$$

where

$$f = \frac{2\omega\cos\theta_k}{\lambda} r \tag{15}$$

and ω is the rotation rate, still to be estimated. A sufficient number of such projections at different angles are required to obtain an image.

The CPIs are not required to be non-overlapping. In fact, numercial experimentation has shown that a certain degree of overlapping between adjacent CPIs, here described by a factor called the *overlapping factor* F, can lead to a smoother tomographic image.

The estimation for the rotation rate ω, which is usually an unknown and constant parameter of the system, can be achieved by a number of different methods of which an iterative procedure based on some quality measure of the resulting image is one possibility. Also, object translational motion compensation must be done prior to the back-projection algorithm processing, which can be implemented simply by shifting the spectrum $S(f,t_k)$ to place the body line (which is also *usually* the strongest line) at zero Doppler before scaling it to form $p_{\theta_k}(r)$.

2.3 Image Resolution and System Requirements

There are a number of factors determining the achievable image resolution and the required system parameters. These include the fundamental limit due to available bandwidth expressed by the point spread function, and various factors involved in the formation of projections. These factors include the finite sampling rate of the radar system, the CPI used for a projection, as well as the rotation speed and cross-range dimension of the object.

2.3.1 The Point Spread Function

In reality, the integration limits and frequency extent are all necessarily finite, and the available 'angular bandwidth' may be less than the full circle. Equation (7) of Section 2.1 must then be replaced by

$$\sigma(x,y) = \int_0^{\pi} \left[\int_{-\infty}^{\infty} W_\theta(f_r)\, |f_r| P_\theta(f_r)\, e^{i2\pi f_r (x\cos\theta + y\sin\theta)}\, df_r \right] d\theta, \tag{16}$$

where $W_\theta(f_r)$ defines the available bandwidth

$$W_\theta(f_r) = \begin{cases} 1, & (f_r,\theta) \in D \text{ (some domain)} \\ 0, & \text{otherwise} \end{cases}\,, \tag{17}$$

and sets the fundamental limit on the resolution of the system. The 2D inverse Fourier transform of $W_\theta(f_r)$ is called the point spread function (PSF), where the PSF becomes more focused as the domain D gets larger, resulting in improved image resolution.

2.3.2 Sampling Rate Requirement

The sampling rate (or pulse repetition frequency (PRF) in narrow-band pulse Doppler radars which collects only one sample per transmitted pulse) needs to be sufficient to cover the entire Doppler frequency extent of the target. More exactly, assuming that the body Doppler line of the object has been shifted to zero frequency, the Doppler frequency of a point scatterer at the largest radius, denoted R_{tip}, from the center of rotation (i.e. the 'tip' Doppler) is

$$f_{tip} = \frac{2v_{tip}}{\lambda}\cos\theta = \frac{2R_{tip}\omega}{\lambda}\cos\theta,$$

which takes maximum values when $\cos\theta = \pm 1$ at $\theta = m\pi$; $m = 0, 1, 2, \ldots$. By the Nyquist criterion, the *minimum* sampling rate to capture the highest Doppler frequency components without aliasing (or ambiguity) is simply

$$PRF_{min} > \frac{4L\omega}{\lambda}. \tag{18}$$

This requirement on sampling rate applies equally to all types of Doppler radar tomography.

2.3.3 CPI Requirement for Fourier Transform Based Systems

In Doppler radar tomography based on the Fourier transform, especially the Fast Fourier Transform (FFT), the length of a coherent processing interval (CPI) is limited by the condition that the rotational motion of a point scatterer on the object must not induce a Doppler spread large enough to spread more than one frequency filter width. This is because the frequency filters translate directly to cross-range bins, and any spread of the signal over more than one filter would translate into cross-range 'walk-off', or smearing, in the resulting image.

Referring to Figure 1, cross range is given by $x = r\cos\theta$, hence the differential change in x is

$$dx = -r\omega\sin\theta\, dt.$$

Maximum cross range walk-off occurs near $\theta = n\pi/2$, with n being an odd integer. If dt represents a CPI time, now denoted by T_{CPI}, then the requirement for no cross range walk-off during a CPI translates to $|dx| = r\omega T_{CPI}$ to be within a cross range bin, for all points along the radial direction r.

With R_{tip} again denoting a largest radial distance of any scatterer on the object relative to the centre of rotation, $N_s = T_{CPI} \times PRF$ being the number of samples used, which is for now assumed to equal to the FFT length, then for the point scatterer center at R_{tip},

it is straightforward to show that the requirement becomes

$$N_s < \frac{PRF}{\omega}\left(\frac{\lambda}{2R_{tip}}\right)^{1/2} = PRF\left(\frac{\lambda}{2\,\omega\,v_{tip}}\right)^{1/2} = \left(\frac{2PRF}{\omega}\right)^{1/2}\left(\frac{PRF}{2\,f_{tip}}\right)^{1/2} \tag{19}$$

as a condition on integration time T_{CPI}, or equivalently the number of samples N_s used for integration, for smear-free projections. If N_s exceeds this limit, resolution in a projection may be improved toward the tips but smearing will result toward its center.

Also from (19), a smear-free CPI time *for each projection* and the corresponding angle of rotation of the scatterer is

$$T_{CPI} = N_s\,PRI = \frac{1}{\omega}\left(\frac{\lambda}{2R_{tip}}\right)^{1/2}, \tag{20}$$

$$\Delta\theta = \omega \times T_{CPI} = \left(\frac{\lambda}{2R_{tip}}\right)^{1/2} \text{(rad)}, \tag{21}$$

which is independent of PRF, but dependent on radar wavelength λ, rotation rate ω and maximum radial extent R_{tip}. With an X-band wavelength and a radial extent between 4 to 10 meters, (21) gives $\Delta\theta$ between 2.2 to 3.5 degrees for each projection.

For the case of absolutely minimum PRF given by (18), the result in (19) gives the required maximum number of samples for no cross range smearing:

$$N_s < \left(\frac{8R_{tip}}{\lambda}\right)^{1/2} \equiv N_{pr}, \tag{22}$$

which is an upper limit independent of the rotation rate. The quantity N_{pr} is also the maximum number of points spanning the cross range extent of the target, free of smearing, if the chosen PRF is not the minimum. It also means that a *fundamental cross range resolution limit*, for Fourier transform based techniques, is

$$dx_{fund} = \frac{2R_{tip}}{N_{pr}} = \left(\frac{\lambda R_{tip}}{2}\right)^{1/2}. \tag{23}$$

Note that this resolution limit is independent of ω and PRF.

2.4 An Example

For a simple example, two rotating point scatterers are positioned at $(-4,-4)$ and $(1,1)$ in the (x,y) plane respectively. They rotate at a rate of 300 RPM about the origin and have the same RCS. The following radar parameters used include a wavelength $\lambda = 0.03$m, $PRF = 26$ kHz, and a dwell time of approximately 0.2 sec (one cycle of rotation).

Figure 2(a) shows the smear-free projections, with no overlapping between adjacent CPIs (i.e. $F = 0$), of two point scatterers rotating about a coordinate origin, with the resulting tomographic image shown in Figure 2(b). While more discussion will be given

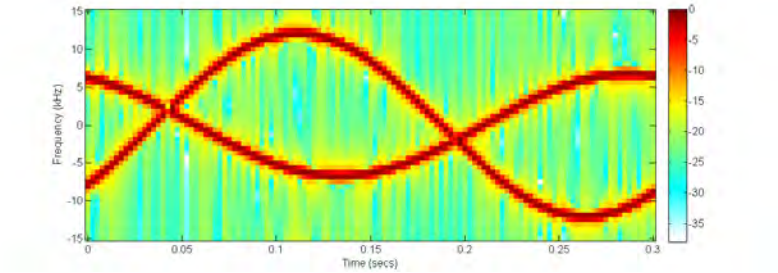

(a) Smear-free projections of two point scatterers with $F = 0$.

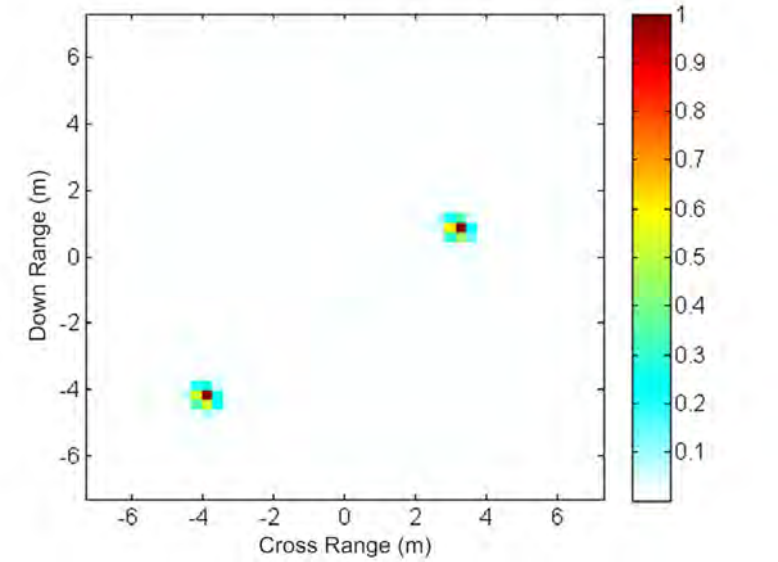

(b) Tomographic image of two point scatterers using the smear-free projections

Figure 2: *Smear-free projections and resulting tomographic image, based on the Fourier transform. Example for two rotating point scatterers rotating at* 300 *RPM, when viewed by an X-band radar* ($\lambda = 0.03$ *m), using* 41 *samples over a* 0.2 *s period.*

in the next section, it suffices here to indicate that, under the smear-free condition, each CPI consists of only 41 samples and the pixel size of this image is approximately 0.29 m by 0.29 m.

If more samples are used in a CPI in an attempt to increase resolution, smearing in the projections and the resulting image occurs, as can be seen in Figure 3. Here, the CPI length is increased from the smear-free case by eight times, while an overlapping factor of 0.6 has been used to obtain a reasonable number of projections for imaging. Figure 3(a) indicates that the frequency spread is most pronounced around zero Hertz (when the scatterer is moving in the pure cross-range direction relative to the radar) and the least at the tip values (when the scatterer's velocity is along the line-of-sight). It should

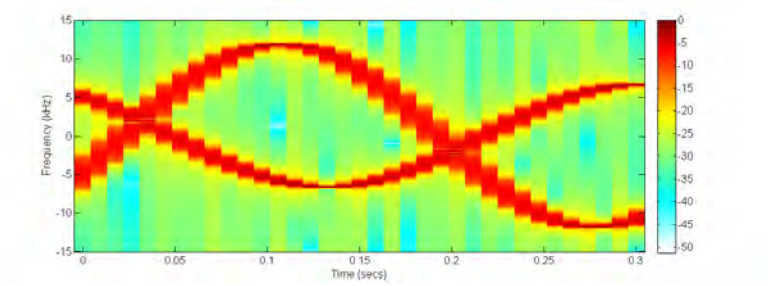

(a) Smeared projections of the two point scatterers, and $F = 0.6$.

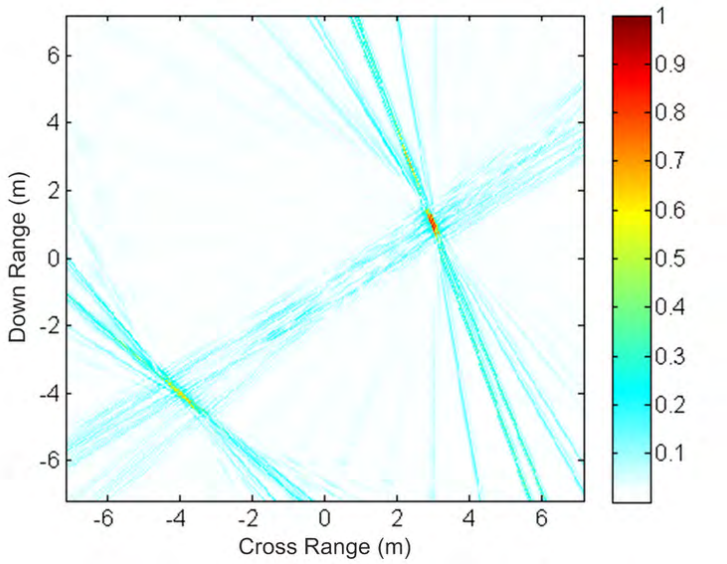

(b) Tomographic image of two point scatterers using the smeared projections

Figure 3: *Smeared projections and resulting tomographic image. The same scatterers as used in Figure 2, using* 328 *(*41×8*) samples over a* 0.2 *s period.*

also be pointed out that 'smearing' in Figure 3(b) means the 'blobs' representing the point scatterers spread over multiple pixels in that figure, compared to the smear-free case, whose overall blob size is smaller. In fact, smearing occurs mostly in the direction tangential to circular path of rotation. This is characteristic of the tomographic processing and partly due to the fact that the tip scatterers are still very well focused in the projections.

It will be shown in the next sections how the FrFT and the S-Method can help overcome this limitation.

3 The FrFT and its Application

This relatively new tool was first proposed by Namias [20] in 1980 in the field of quantum mechanics, which has been discussed extensively by many authors for applications in signal processing only the last fifteen years or so [13, 14, 15, 16, 17, 18]. As a generalisation of the traditional FT in a rotated time-frequency plane, it has great potentials in the analysis of chirp signals which become 'pure tone' signals in appropriately rotated time-frequency frames. It has been used to analyse and extract multiple linear frequency modulated (LFM) audio signals from bats by Capus *et al.* in [11]. It has also been applied to the SAR and ISAR imaging problems of moving and maneuvering targets by various authors [21, 22, 23, 24]. The detection of accelerating targets in clutter is another obvious application that the FrFT can be expected to perform well, and is a topic for future reports.

In our problem of Doppler radar tomography, the time signal in a CPI, in many cases, can be described as the sum of a number of quasi-LFM signals, and thus the FrFT can be effective in its analysis. In particular, if the LFM signals can be extracted and spectrally compressed separately using a bilinear transform such as the S-Method, then the problem with spurious components with overlapping signals can be resolved, and thus improved image resolution can be achieved.

3.1 A Definition of the FrFT

Given a time signal $s(t)$, its FrFT is defined as

$$S_\alpha(u) = \mathcal{F}_\alpha\{s(t)\} = \int_{-\infty}^{\infty} K(\alpha, u, t)\, s(t)\, dt, \tag{24}$$

where the kernel function is

$$K(\alpha, u, t) = \begin{cases} \left(\frac{1-i\cot\alpha}{2\pi}\right)^{1/2} \exp\{i\frac{\cot\alpha}{2}(u^2+t^2)\} \exp\{-i\frac{u}{\sin\alpha}t\}, & \alpha \neq n\pi, \\ \delta(t-u), & \alpha = n2\pi, \\ \delta(t+u), & \alpha + \pi = n2\pi, \end{cases} \tag{25}$$

and where α is called the *order* of the transform, which can also be interpreted as an angle of rotation in the time-frequency plane.

For $\alpha = 0$ (i.e for $n = 0$ in Equation 25), we have $S_0(u) = s(u)$ which is the time-domain signal itself. For $\alpha = \pi/2$, we have $\cot\alpha = 0$ and $\sin\alpha = 1$, and $S_{\pi/2}(u)$ reduces to the classic Fourier transform $S(u) = S(f)$ of $s(t)$. *It is insightful to re-interpret the classic FT as a rotation of the time signal through an angle of $\pi/2$ in the time-frequency plane.* A rotation through some other angle gives a generalised or 'fractional frequency' spectrum of the signal at that angle, with the fractional frequency denoted by u[1].

The *inverse* FrFT is simply the rotation of the $S_\alpha(u)$ through an angle of $-\alpha$, such that

$$s(t) = \int_{-\infty}^{\infty} K(-\alpha, u, t)\, S_\alpha(u)\, du. \tag{26}$$

where $S_\alpha(u) = \mathcal{F}_\alpha\{s(t)\}$.

[1]For this reason, the same notation $\mathcal{F}$ is used for both the classic Fourier transform and the fractional Fourier transform, with a subscript α explicitly denoting the 'fractional form'.

3.1.1 Properties of the FrFT

Some properties of the FrFT of order α, which are most relevant to the present work, are summarised below:

1. $$s(u) = \mathcal{F}_0\{s(t)\} \tag{27}$$

   The time-signal is its own FrFT at order zero.

2. Rotation to the classic Fourier transform

   $$S(f) = \mathcal{F}_{\pi/2}\{s(t)\} = \mathcal{F}\{s(t)\} \tag{28}$$

   The classic Fourier transform is the FrFT at order $\pi/2$.

3. Cumulative rotation. If $\alpha = \alpha_1 + \alpha_2$, then

   $$S_\alpha(u) = \mathcal{F}_{\alpha_2}\{\mathcal{F}_{\alpha_1}\{s(t)\}\} = \mathcal{F}_{\alpha_1}\{\mathcal{F}_{\alpha_2}\{s(t)\}\}. \tag{29}$$

   Successive rotations add up.

3.1.2 Computation of the FrFT

We have used a computational algorithm proposed by Ozaktas *et al.* as described in [12] for the computation of $S_\alpha(u)$ in (24), which can be summarised as follows.

1. First, the kernel function $K(\alpha, u, t)$ in (25), for the cases of $\alpha \neq n\pi$, is re-expressed in a form which is numerically more stable:

   $$K(\alpha, u, t) = A_\alpha \exp\left\{-i\pi\left[u^2 \tan(\frac{\alpha}{2}) - \beta(u-t)^2 + t^2 \tan(\frac{\alpha}{2})\right]\right\}, \tag{30}$$

   where $A_\alpha = [(1 - i\cot\alpha)/2\pi]^{1/2}$, $\beta = 1/\sin\alpha$, and u is now in units of Hertz if $\alpha = \pi/2$.

2. Set a value for α and initialise (and discretise) the time vector $t \in [0, t_{CPI}]$. α can be restricted to an interval of values corresponding only to practically realistic chirp rates;

3. Multiply the original time signal $s(t)$ with the chirp term in the time domain, $\exp\{-i\pi t^2 \tan(\alpha/2)\}$, ensuring that a sufficient level of interpolation and decimation is used to cover the increased bandwidth brought about by the chirp factor;

4. Convolve the above output with $\exp\{-i\pi\beta t^2\}$;

5. Finally, multiply the above output with the chirp term in the u domain and the complex factor A_α.

3.2 Application of the FrFT

3.2.1 Spectral Composition of a Projection

Figure 4 depicts the 'chirp content' of a projection in our Doppler tomography problem in which target range is very large compared to the radius of the rotational motion. Theoretically, each scattering center of a rigid target traces out a sinusoid in the time-frequency plane with the same angular rate but generally different amplitudes and phases (which depend on the relative position of that center in the target), and there can be many such sinusoids. The number of chirps in a projection is equal to the number of point scatterers present in that CPI.

With the classic FT, a projection at a particular point in time can be represented as the FT spectrum obtained from that CPI. The longer the CPI, the higher resolution can be achieved in the spectral domain but the frequency variation of the chirps also deviates more from the LFM approximation. More importantly, with the classic FT, which is a projection of the signal onto the frequency axis (see Figure 4), the chirps may significantly spread and overlap among themselves. With the FrFT, one or more chirps may have their spread much reduced in the u-domain, if a good estimate of α is used for the FrFT, and thus separation from the rest of the signal may be possible.

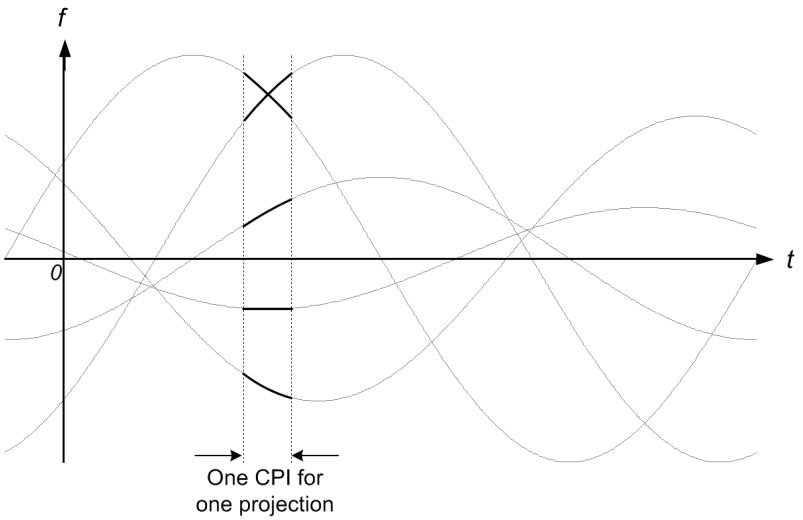

Figure 4: *A projection may contain many different chirps*

To spectrally compress a chirp with chirp rate c_r and its instantaneous frequency in the form $f = f_0 + c_r t$, the optimal transform order α that should be used is related to c_r through

$$\alpha = \frac{\pi}{2} + \tan^{-1}(D\, c_r), \tag{31}$$

in which the scale factor D due to the discretisation of the time-frequency domain is related to the time and frequency resolutions δt and δf by [15]

$$D = \left(\frac{\delta f}{\delta t}\right)^{-1} = \left(\frac{N_s}{PRF^2}\right). \tag{32}$$

With the angle of rotation expressed in (31), the signal would appear like a 'pure tone' along the 'fractional time' domain, or equivalently as an optimally compressed spike in the 'fractional frequency' domain.

3.2.2 FrFT Application

Since there are many chirps of different chirp rates present in a projection, a number of rotations of the time-frequency plane may be required for each CPI. Note that while the instantaneous Doppler frequency of a point scatterer, $(2\omega/\lambda)x$, is determined by the cross range x, chirp rate (derivative of frequency) is $(-2\omega^2/\lambda)y$, determined by the down range y as seen in Figure 5. The down range extent of targets of interest is finite, suggesting a finite range of possible values over which to search for the 'best' or 'close enough' chirp rates.

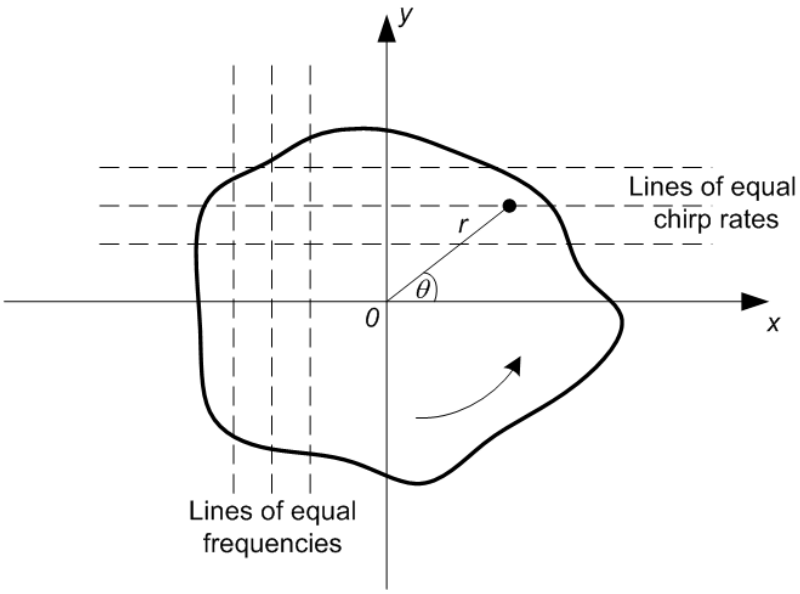

Figure 5: *Lines of equal Doppler frequency (in cross-range) and lines of equal chirp rates (in down-range).*

The relevant chirp rate interval may be sampled by a finite number of values of c_r. At each value, the fractional spectrum is searched for the most spectrally compressed peak.

An illustration of the evolution of the FrFT for different α values is shown in Figure 6. The smearing of the spectrum from the two LFM signals and the focusing of each spectral line as the order of the transform, α, is well matched with the chirp rate of the LFM signal, which occur at $\alpha = 84.7^o$ and $\alpha = 93.3^o$, can be seen. The traditional FT results when $\alpha = 90^o$, as discussed earlier. Here, we have used the following system parameters: $\lambda = 0.03$ m, $PRF = 30$ kHz, rotation rate = 300 RPM, scatterer 1 position $(x, y) = (1, 1)$ and scatterer 2 position $(x, y) = (-1, -1)$.

A search algorithm is required to determine when the optimum focusing of a spectral line occurs, which is then extracted by setting the fractional spectrum at all other u

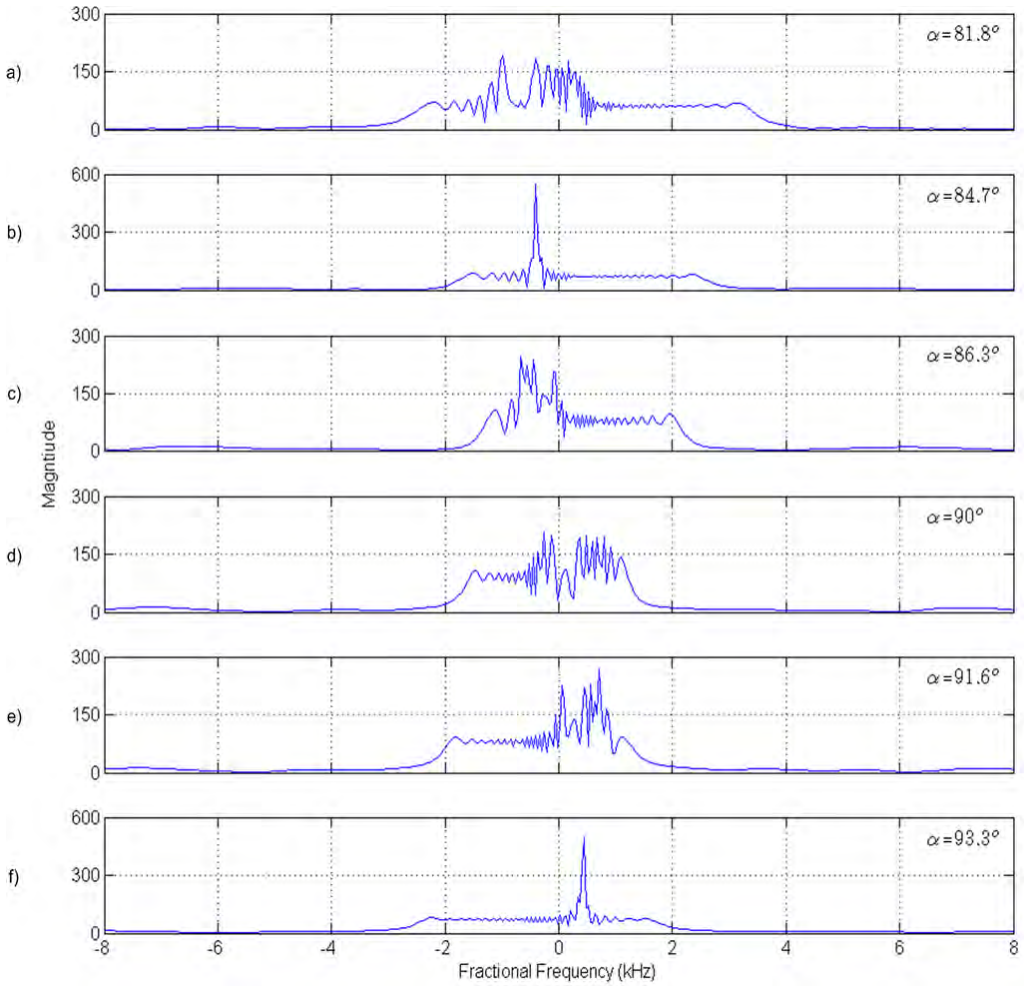

Figure 6: *Evolution of the FrFT spectrum of two chirp signals.*

outside the focused peak to zero and *rotated to* $\alpha = \pi/2$ (the physical frequency domain). The remaining portion of the fractional spectrum is rotated to the next value of α and the process is repeated, until all chirp rate values have been searched. A more detailed description of the algorithm is presented in Section 5. All extracted chirps are then spectrally compressed using the S-Method described in the next section.

The search and extraction function is not discussed in detail in this report as it continues to be an area of research and will be addressed in future publications.

4 The S-Method and its Application

In the present algorithm, the S-Method is used to spectrally compress a LFM signal, after it has been extracted by the FrFT described above. The S-Method was first proposed by L. Stankovic [19] in 1994 and has since been applied to many problems in micro-Doppler signal analysis by T Thayaparan *et al.* [6]. In the following, we summarise its basic theory and discuss the necessary modification for its application to Doppler radar tomography.

4.1 Description of the S-Method

The S-Method as proposed by Stankovic is basically a Wigner distribution[2] (WD) modified with a reduced integration extent.

While the Fourier transform is a linear transform of a signal $s(t)$, the Wigner distribution is a second-order, or bilinear transform, and is defined (in the analog pseudo form) as

$$S_{WD}(f,t_k) = \int_{-\infty}^{\infty} w(t/2)w(-t/2)\, s(t_k + t/2)s^*(t_k - t/2)e^{-i2\pi ft}\, dt. \tag{33}$$

It is known that the Wigner distribution is ideal for a single LFM signal, in the sense that the spectral spread caused by the frequency modulation as seen in its Fourier transform $S(f,t_k)$ is completely removed, and its Wigner distribution $S_{WD}(f,t_k)$ is identical to the spectrogram of a pure sinusoid. For multiple LFM signals, however, the usefulness of the Wigner distribution is much reduced by the existence of strong cross terms.

The Wigner distribution $S_{WD}(f,t_k)$ can also be expressed in terms of the short-time Fourier transform $S(f,t_k)$ as

$$S_{WD}(f,t_k) = \frac{1}{\pi}\int_{-\infty}^{\infty} S(f+f',t_k)\, S^*(f-f',t_k)\, df', \tag{34}$$

which can be readily verified by, for example, directly substituting the definition of $S(f,t_k)$ as expressed in (13)[3]. To avoid cross terms, at least when the auto-terms are reasonably separated in frequency, the S-Method, in its analog form, is then defined as

$$S_{SM}(f,t_k) = \frac{1}{\pi}\int_{-f_L/2}^{f_L/2} S(f+f',t_k)\, S^*(f-f',t_k)\, df', \tag{35}$$

where f_L is a finite real number, representing a finite frequency extent of integration centered around the frequencies of the component LFM signals.

In discrete form, the S-Method transform is written as

$$S_{SM}(n,k) = \sum_{i=-L}^{L} S(n,k+i)\, S^*(n,k-i), \tag{36}$$

where L is an integer to be chosen. When $L = 0$, the S-Method reduces to the spectrogram. When L spans the entire discrete Fourier domain, the S-Method is identical to the Wigner distribution. L can be chosen to vary with frequency filter index k, and since the aim is to optimise the focusing (or spectral compression) of the auto-terms and to avoid the cross terms, L needs to be determined adaptively for each value of k. In the present work, the criterion used is that, for a 'simple hump' in the STFT, the sum in (36) stops when either $|S(n,k+i)|$ or $|S(n,k-i)|$ is less than a certain percentage of the nearest local maximum. For multiple humps, we have used an improved criterion (not described here) which produces an L-profile such as in Figure 8.

[2] which is also known as "'Wigner-Ville Distribution"'

[3] Assuming the integration extent in (13) is from $-\infty$ to $+\infty$ and using the property of the Dirac δ function.

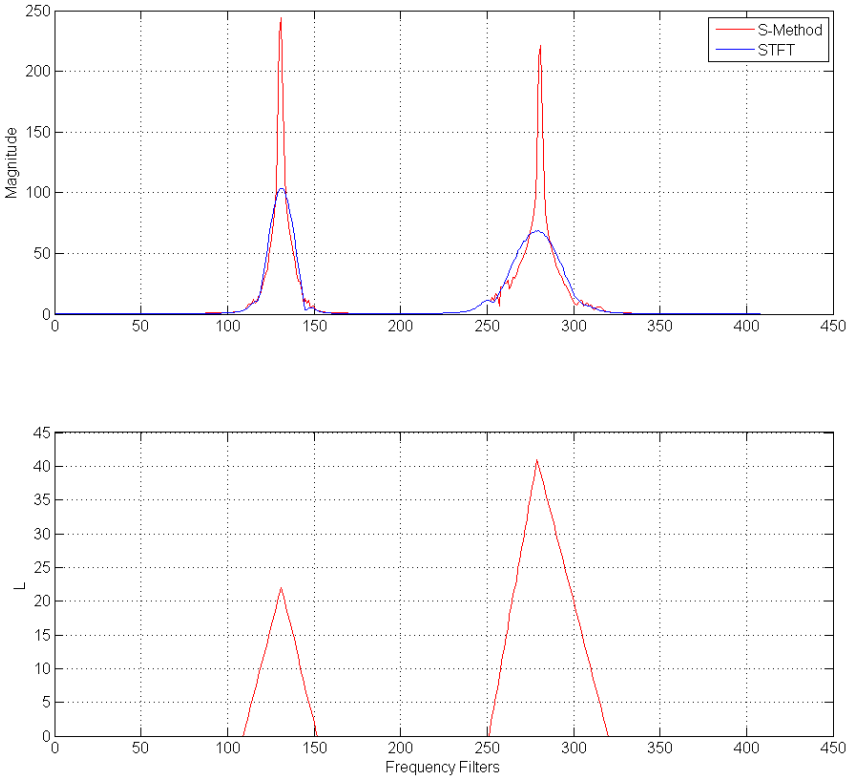

Figure 7: *Demonstration of the compression performance of the S-Method technique, a) S-Method and FFT comparison, b) the L profile.*

More importantly, to obtain a projection for tomographic imaging and preserve its first-order dimensionality, we also make a simple modification of the 'conventional' S-Method by taking the *square root* of the above sum:

$$S_{SM}(n,k) = \left[\sum_{i=-L}^{L} S(n,k+i)\, S^*(n,k-i) \right]^{1/2}. \tag{37}$$

This modified S-Method may appropriately be called *the tomographic S-Method.*

4.1.1 Example: Implementation of the S-Method

An example of a smeared spectrum, the 'spectral compression effect' of the S-Method and the L profile is shown in Figure 7. Note in this figure that the L profile is necessarily larger for a more spread LFM signal (on the right) than for the less spread signal (on the left). When a signal is already strongly peaked, no L profile is necessary.

4.1.2 Limitation of the S-Method

The S-Method works well for the above example, when the two chirp signals are well separated in frequency. When the two chirp signals strongly overlap, which is certainly

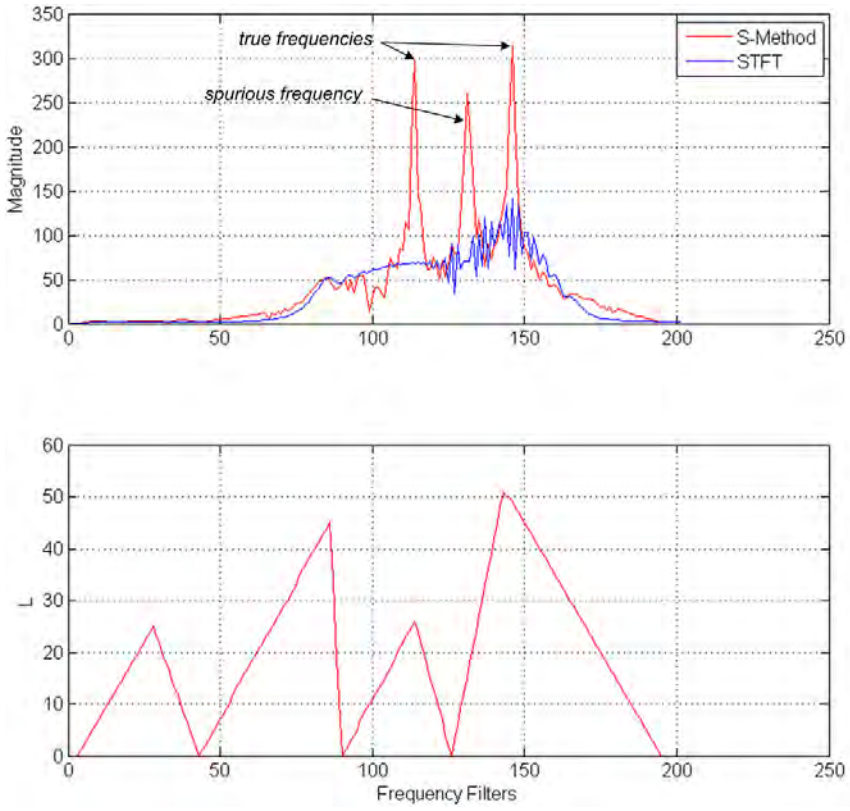

Figure 8: *The compression performance of the S-Method technique for multiple, closely spaced terms, a) S-Method and FFT comparison showing unwanted cross-terms, (b) the L profile.*

the case when two scattering centers roughly line up in the radar line-of-sight, spurious frequency components arising from cross terms, which become a nuisance leading to a degradation in the final tomographic image. This undesirable effect is illustrated in Figure 8. In general it is desirable to apply an extraction step using the FrFT prior to the application of the S-Method.

5 Algorithm for Chirp Extraction and Compression

This section describes the algorithm proposed and employed in this work, for improving the resolution of a tomographic image using the fractional Fourier transform and S-Method. Figure 9 shows a flow chart of the algorithm which is described in more detail below, with Figure 10 providing descriptive support.

Step 1: *Collect time signal data for a CPI.* Data from the time signal is collected for a CPI, with an example shown in Figure 10(a).

Step 2: *Calculate the chirp rate and α value.* The first chirp rate is calculated based on a reasonable assumption of the objects down range extent and the associated α is calculated

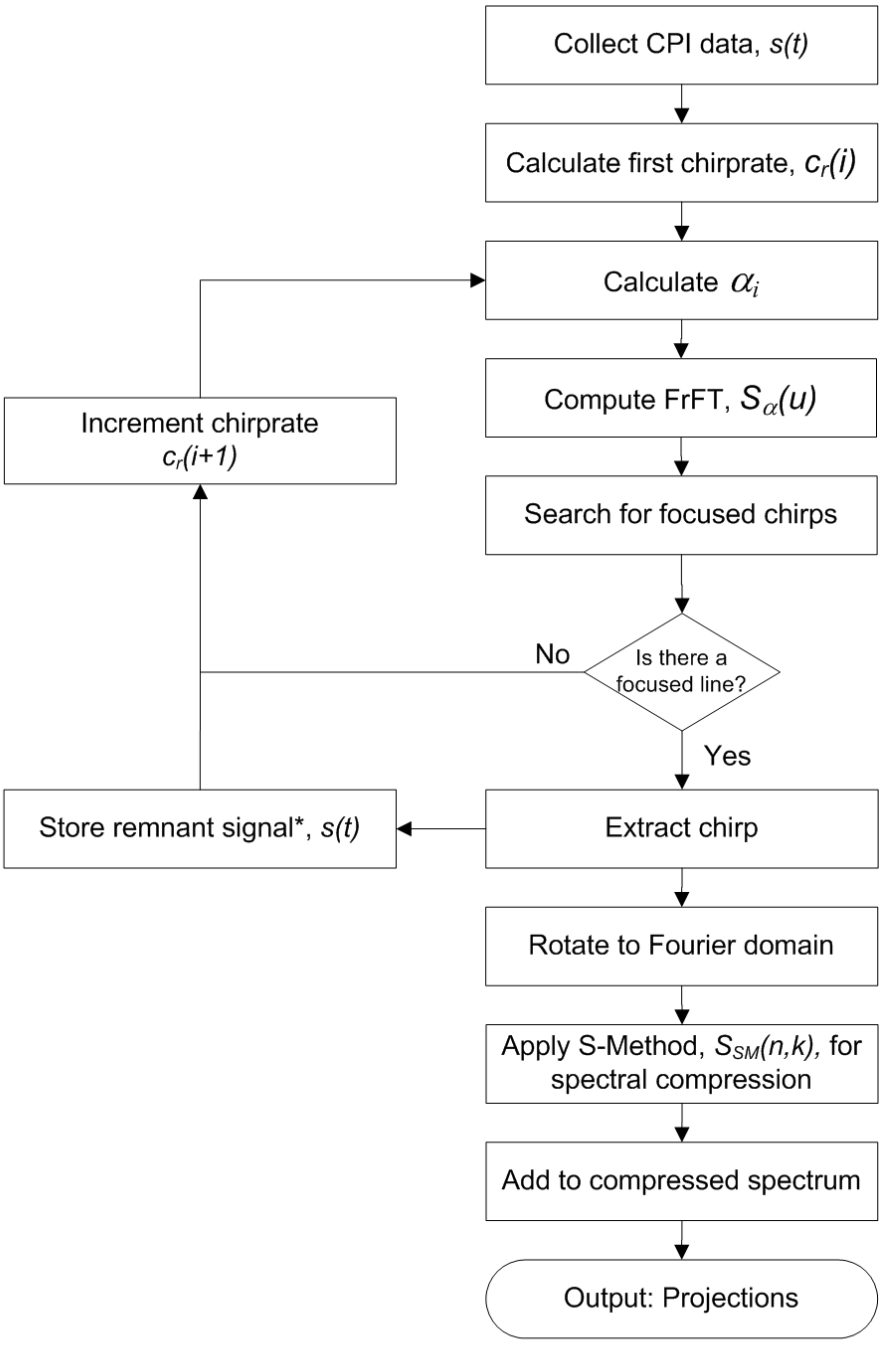

Figure 9: *A flowchart to describe the processing steps to apply the FrFT and S-Method algorithms to data to improve projection resolution.*

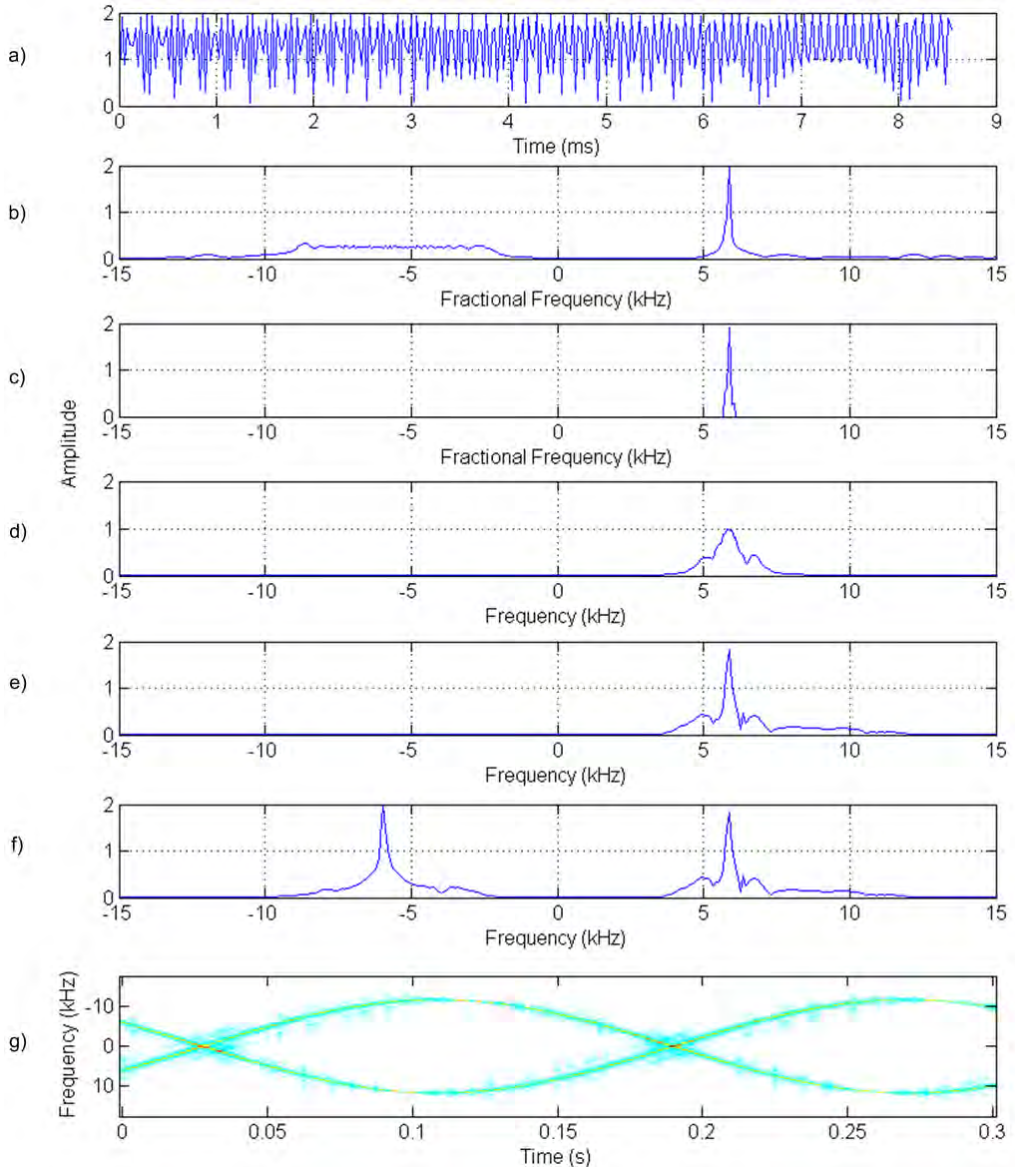

Figure 10: *FrFT and S-Method algorithm description showning the process steps, a) the time-domain signal for a CPI interval, b) FrFT revealing a compressed chirp and uncompressed chirps, c) extracted compressed chirp, d) FrFT chirp rotated to the Fourier domain, e) S-Method applied to chirp, f) S-Method applied to all chirps in CPI, g) resulting compressed time-frequency (projections) plot for all CPI.*

using Equation 31.

Step 3: *Compute FrFT and chirp search.* For the calculated α, the fractional Fourier transform is applied to the data. The resulting fractional spectrum is searched for focused chirps, or compressed spectral lines. Figure 10(b) shows an example of a fractional spectrum with a compressed chirp. If the resulting spectrum does not contain a compressed spectral line then return to step 2 for the next chirp rate value. (The actual algorithm for determining the existence of a compressed spectral line is not discussed here and will be

discussed in a separate report.)

Step 4: *Chirp extraction.* If a focused line exists, the extent of this line is extracted giving a new spectrum as seen in Figure 10(c), which continues to be processed by steps 5 to 7 below. The remnant signal goes back to step 2 with the next chirp rate value, until all chirp rates have been searched.

Step 5: *Rotate to the classic frequency domain.* At the input to this stage, the extracted chirp is still in the fractional frequency domain and must be rotated to the physical frequency domain. Its resulting spectrum is an uncompressed chirp as shown in Figure 10(d).

Step 6: *Apply the S-Method.* The S-Method can now be applied to the single chirp spectrum to refocus the spectral content. The ability of the S-Method to properly focus the chirp is improved by the isolation of chirps. The resulting S-Method compressed spectrum is shown in Figure 10(e).

Step 7: *Compute the Projections.* The isolation and extraction of chirps in the signal are applied for all chirp rates and the S-Method compression is applied to each. The final projection is a sum of all compressed spectra, as shown in Figure 10(f), for a given CPI.

The processing steps described above are repeated for all CPI's to give focussed projections for all aspect angles, as exemplified in Figure 10(g), used later for tomographic imaging. Note that the best estimate of the chirp rate and therefore of the rotation rate, ω, can be determined by a refinement of step 2. However, this is not the goal of this current work.

6 Algorithm Performance Results

This section aims to demonstrate the performance of the proposed image resolution improvement algorithm on chirped signals. The demonstration uses 3 types of processing. The first type uses an optimal number of samples, N_s, that gives no smearing, but relatively low resolution, in the traditional Fourier transform based scheme. The second type uses a number of samples several times greater than N_s, producing a smeared image. The third type has the new algorithm applied to the smeared signal to produce a high-resolution image.

The demonstration is first applied to rotating point-scatterers orientated in a variety of configurations, and in the presence of noise, and then to real helicopter data.

6.1 Point-scatterer Model Target

6.1.1 Noise-free Performance

This section will present several examples to demonstrate the improved resolution and performance of the algorithm, in the case of no additive noise in the received signal. Table 1 shows the radar and object parameters used for generating smear-free and smeared projections.

Table 1: *Table of radar and object parameters for smeared and smear-free projection generation.*

Radar and Object Parameters	
Carrier Frequency (GHz)	10
Pulse Repetition Frequency (kHz)	35
Dwell Time (s)	0.3
Rotation Rate (RPM)	300
Maximum Blade Length (m)	6
Tip Doppler (kHz)	12.56

Smear-free Parameters	
Number of samples, N_s	57
T_{CPI} (ms)	1.6
$\Delta\theta$ (deg)	3

Smeared Parameters	
Number of samples, N_s	456
T_{CPI} (ms)	13
$\Delta\theta$ (deg)	23

Smear-free and smeared projections and associated tomographic images

A set of 4 rotating point scatterers orientated in a square separated by 8 m, is shown in Figure 11(a). The projections were calculated using the value of N_s, given by Equation 19, leading to the time-frequency plot in Figure 11(b). Here we can see the four sinusoids as they rotate over time. Figure 11(c) shows the resulting tomographic image, giving four points in the image. The low value of N_s gives a rather low resolution image but free of smearing.

Figure 12(a) and Figure 12(b) show the smeared projections and resulting smeared tomographic image. The high number of samples, $8 \times N_s$, used for a projection gives a finer image but the longer integration time produces frequency smearing causing the points in the image to be smeared in the tangential direction.

Figure 12(c) and Figure 12(d) shows the improved projections and resulting tomographic image after the fractional Fourier transform and S-Method algorithm is applied to the smeared projections to focus the chirps in the signal. As can be seen, the smearing effect is removed giving 4 sharp points in the image. This allows us to use longer processing intervals, giving greater frequency resolution, without smearing in the image.

To demonstrate in more detail the improvement using the proposed FrFT and S-Method algorithm, Figure 13 shows smeared focused projections containing 2 point scatterers for three CPI's, especially when the spectra of the point scatterers become more and more overlapped. As can be seen, no spurious components are created. Other illustrative examples are provided below.

Example 1: *Closely-spaced point scatterers near the center of rotation.* A set of rotating point scatterers orientated in a square, starting at the origin and separated by 0.5 m, is

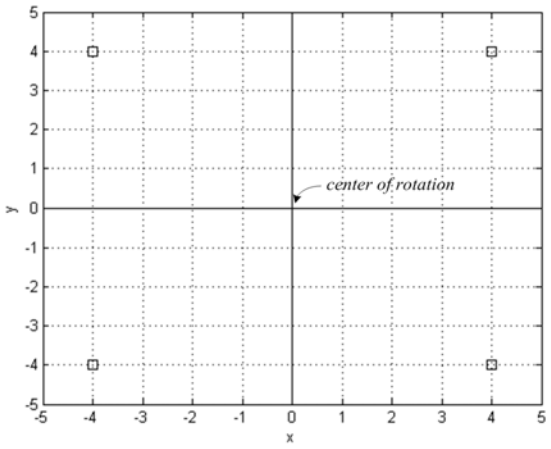

(a) Scatterers orientation

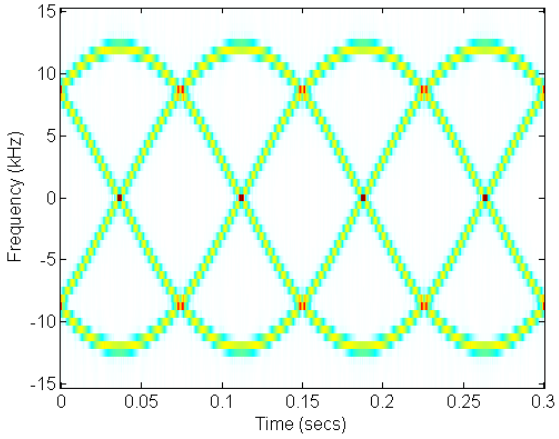

(b) Smear-free time-frequency plot.

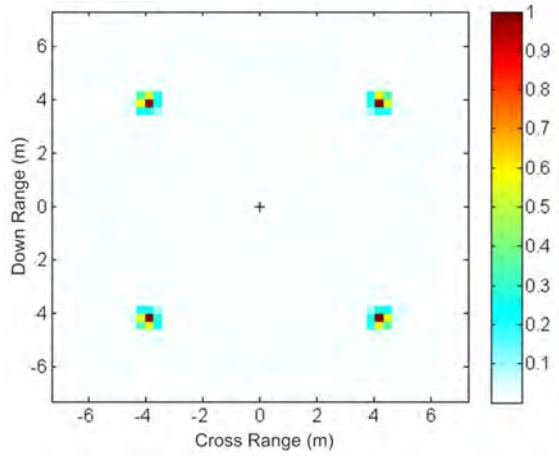

(c) Smear-free tomographic image.

Figure 11: *Projections and tomographic image using the smear-free Ns.*

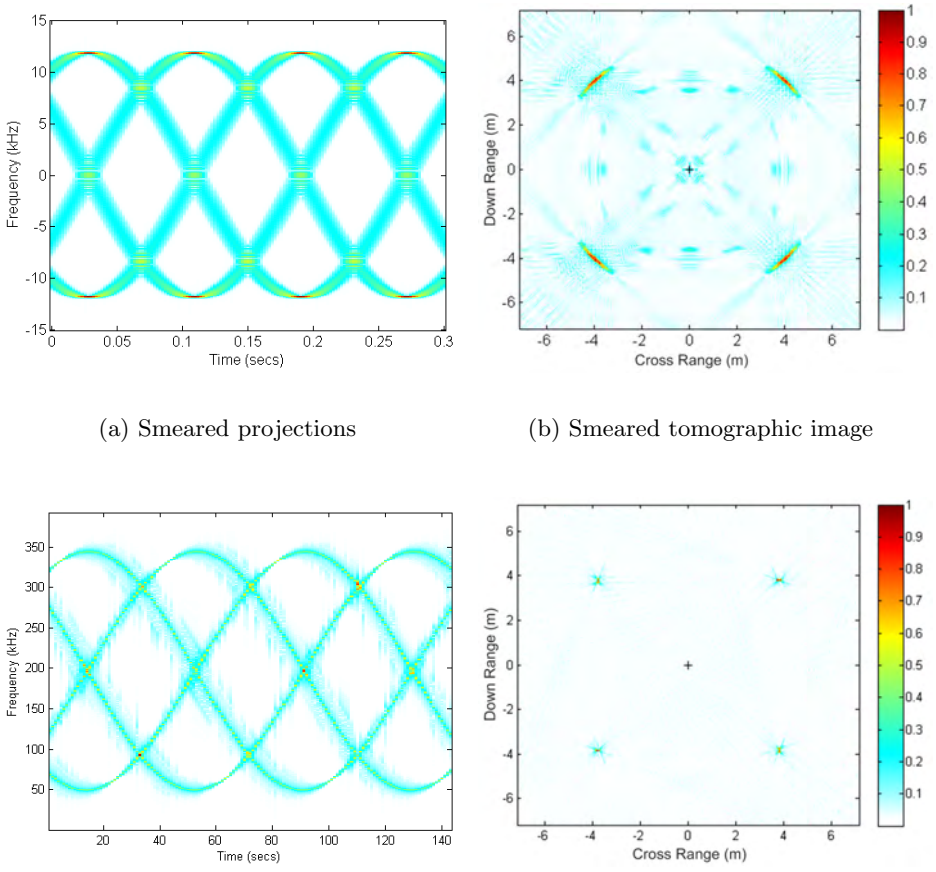

(a) Smeared projections

(b) Smeared tomographic image

(c) FrFT and S-Method improved projections

(d) FrFT and S-Method improved tomographic image

Figure 12: *Smeared and FrFT S-Method improved projections and tomographic image.*

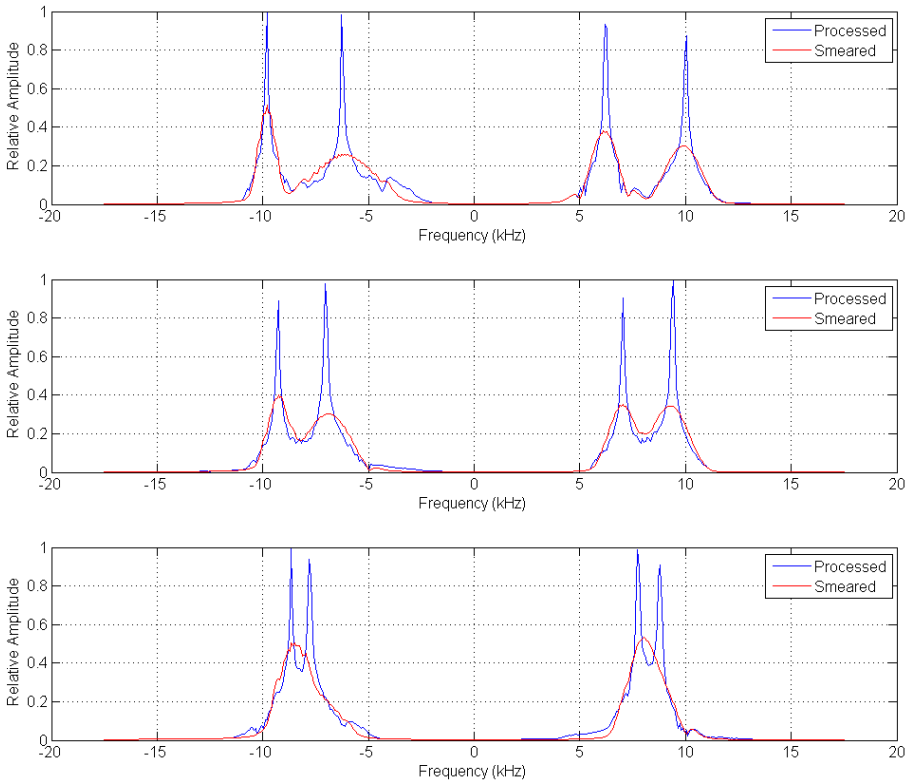

Figure 13: *Smeared and FrFT S-Method improved projections at three CPI's, showing the improvement in resolution and ability to resolve closely spaced scatterers.*

shown in Figure 14(a). The smear-free tomographic image is shown in Figure 14(b). As expected we seen four low resolution scatterers. The smeared tomographic images are shown in Figure 14(c). As can be seen, the scatterer at the origin, having no radial extent (i.e. at the center of rotation), gives no smearing and the overall quality of the image is poor. Figure 14(d) shows the FrFT and S-Method improved tomographic image, giving four points in the image. The proposed algorithm can easily focus 4 closely spaced point scatterers.

Example 2: *Closely-spaced point scatterers offset from the center of rotation by 4 m.* We offset the square by a radius of 4 m as shown in Figure 15. The low resolution in the smear-free image gives no information about the number of scatterers or the scatterer position as seen in Figure 15(b). The smeared image caused by the large radial extent, causes extensive interference of the closely spaced scatterers giving a smeared tomographic image that also doesn't resemble the scatterer positions. The improved image after processing, distinctly shows the scatterers with high enough resolution to confidently resolve the scatterers positions.

Example 3: *Linearly spaced rotating point scatterers orientated tangentially to the direction of rotation.* In this example, a set of 4 point scatterers in a linear pattern orientated tangentially to the path of rotation, separated by 0.2 m, as shown in Figure 16(a). Here we position the scatterers such that the separation cannot be resolved using the smear-free projections, as seen in Figure 16(b), and smeared projections give an image with heavily

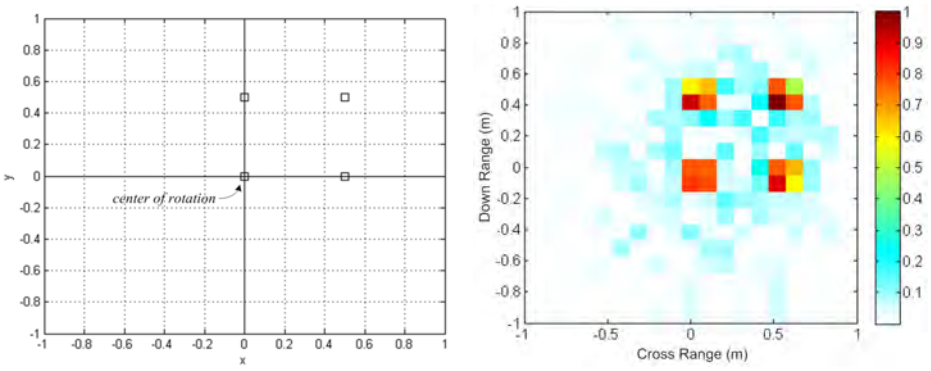

(a) Scatterers orientation

(b) Smear-free tomographic image

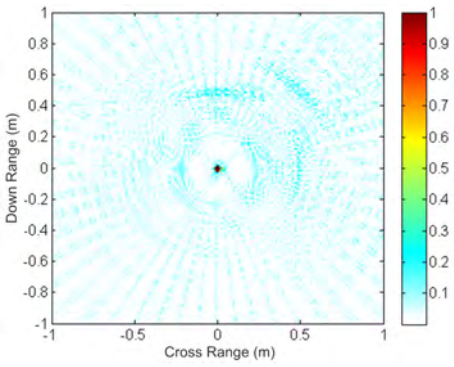

(c) Smeared tomographic image

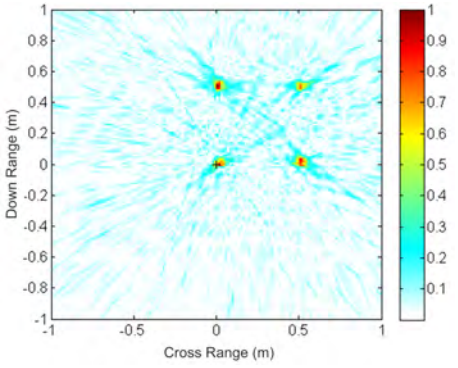

(d) FrFT and S-Method improved tomographic image

Figure 14: *Smeared and improved tomographic images for closely spaced rectangularly orientated rotating point scatterers*

overlapping points, which is indeed the case as seen in Figure 16(c). The improved image, shown in Figure 16(d), demonstrates the excellent performance of the proposed algorithm even for scatterers position 0.2 m apart and in a tangential configuration that would be most smeared in conventional FT-based processing.

Example 4: *Point scatterers orientated in an ellipse offset from the center of rotation.* A set of 10 point scatterers orientated in an ellipse offset from the center of rotation is shown in Figure 17(a). The smear-free image seen in Figure 17(b), shows the position of the scatterers but at low resolution. Using the longer integration time (Figure 17(c)) to improve resolution, the smeared image shows how smearing increases as the scatterer radial extent increases, with closely spaced scatterers further away from the center of rotation overlapping. The FrFT and S-Method processed projections gives an improved tomographic image (Figure 17(d)) showing the scatterers positions with higher resolution.

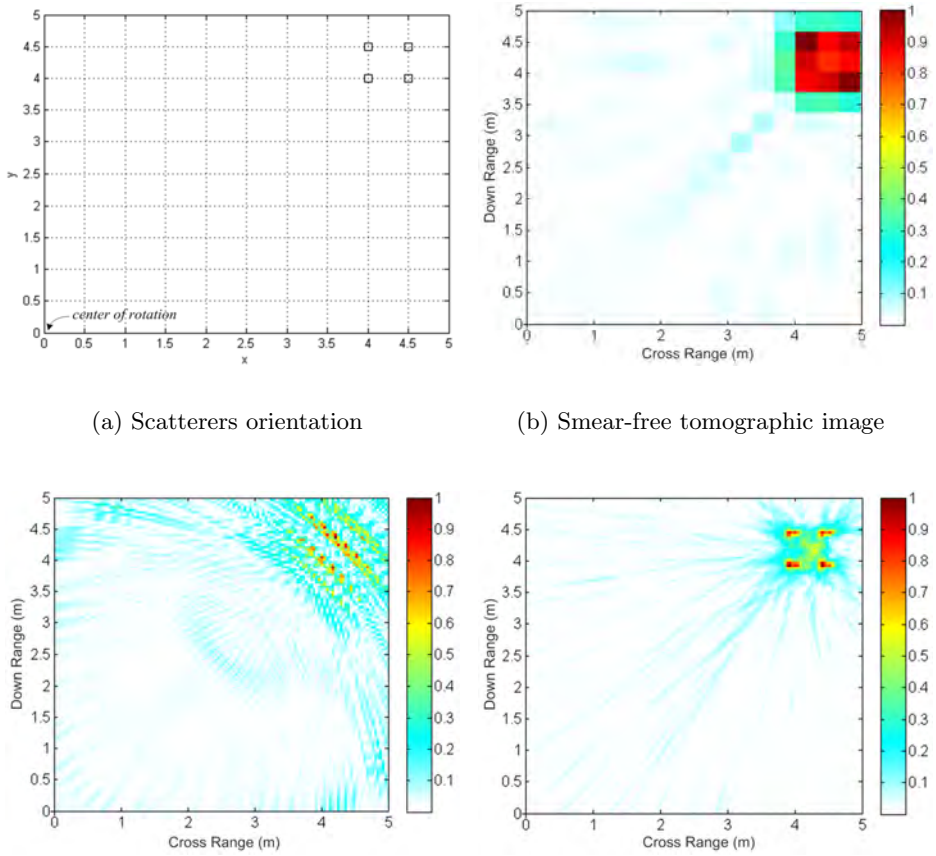

(a) Scatterers orientation

(b) Smear-free tomographic image

(c) Smeared tomographic image

(d) FrFT and S-Method improved tomographic image

Figure 15: *Smeared and FrFT S-Method improved tomographic images for closely spaced square, offset by 4m*

6.1.2 Algorithm Performance in the Presence of Noise

In this section, the FrFT and S-Method algorithm is tested in the presence of noise. Noise samples are added to the time-domain data samples and are modelled as

$$s(t) = s_0(t) + n(t) \tag{38}$$

where $s_0(t)$ is the noise-free signal and $n(t)$ is Gaussian i.i.d. noise samples quantified using the signal-to-noise ratio (SNR).

Using the scatterer orientation shown in Figure 11(a), the processed tomographic image is presented for varying SNR. Figure 18(a) and 18(b) show the smeared and processed tomographic images respectively for a $SNR = 0$dB. The amount of detail in the smeared image is hard to see with the naked eye with the smearing reducing the dynamic range of the image. Its almost impossible to determine the position of the four scatterers. However, the scatterers are easily seen in the processed image for this level of noise. This can be explained by the greater integration time ($8 \times N_s$) used with the proposed algorithm.

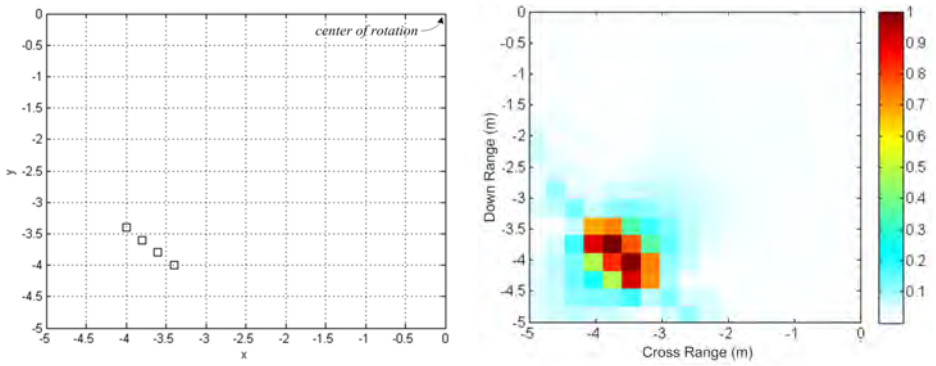

(a) Scatterers orientation

(b) Smear-free tomographic image

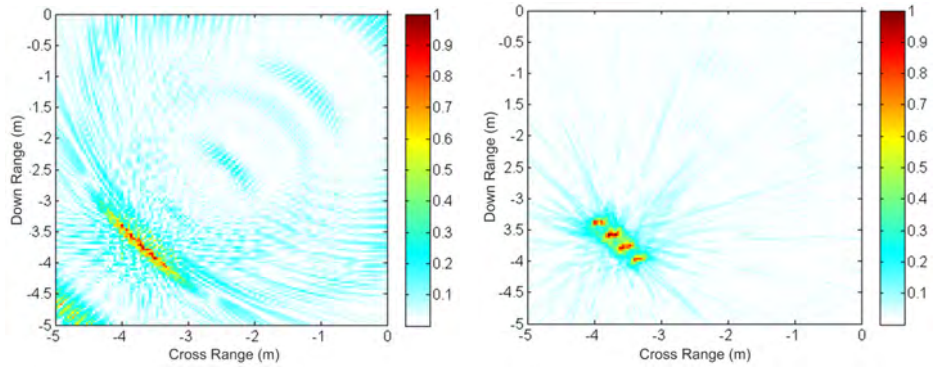

(c) Smeared tomographic image

(d) FrFT and S-Method improved tomographic image

Figure 16: *Smeared and FrFT S-Method improved tomographic images for closely spaced linear orientated scatterers perpendicular to center of rotation*

Figure 18(c) shows the processed tomographic image for a $SNR = -4$dB. The smeared image shows no detail and the scatterers are difficult to see. The image is starting to degrade with scatterer position becoming less defined. Figure 18(d) shows the processed tomographic image for a $SNR = -6$dB. Here we see a degradation of image quality and total destruction of scatterer information.

The FrFT and S-Method algorithm performs well in de-chirping the projections and giving a high resolution image. The algorithm, however, relies on determining when a chirp is compressed, which is Step 3 in Section 5 of the algorithm description. Further work in this area is continuing to maximise the robustness and performance of the algorithm.

Also, this analysis used an integration time such that the number of samples used is 8 times the smear-free N_s. It can be argued that by increasing this integration time, say to $16 \times N_s$, further performance in noise can be achieved. However, on implementing this, no improvement in image quality was seen, with signals with a $SNR = -6$dB still giving a degraded image. The reason for this is the deviation from the LFM assumption as we

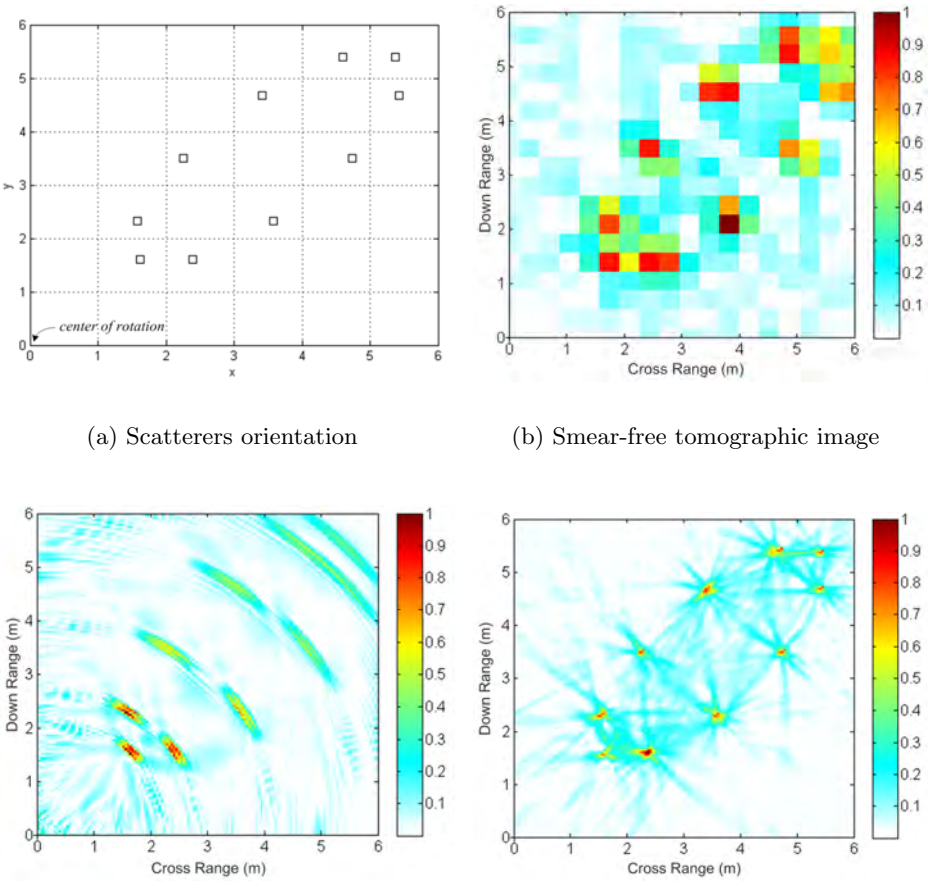

(a) Scatterers orientation

(b) Smear-free tomographic image

(c) Smeared tomographic image

(d) FrFT and S-Method improved tomographic image

Figure 17: *Smeared and FrFT S-Method improved tomographic images for point scatterers orientated in an ellipse offset from the center of rotation.*

increase the integration time and move into the more sinusoidal FM part of the chirp.

6.2 Real Helicopter Data

In this section, we apply the proposed algorithm to real data of a couple of helicopters, despite the fact that a robust algorithm for detailing and tracking focused 'humps' of scatterers is not yet available. The radar return from a helicopter, apart from that of the helicopter body itself, consists of LFM chirp signals from the rotating rotor blades with the return from a blade body dominating when orthogonal to the radar line-of-sight. In fact, due to the shape of the rotor blade tips, the return from the blade tip is consistent for a wide range of aspect angles and is indicative of a rotating point scatterer described earlier. Hence the techniques and FrFT S-Method algorithm described can be applicable to real helicopter data in an attempt to image the blade tips. The two helicopter data sets used for this investigation are shown in Table 2.

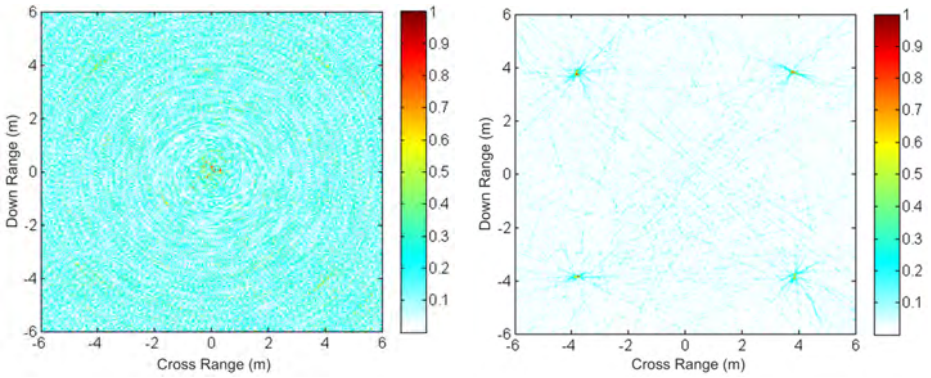

(a) Smeared tomographic image with $SNR = 0$dB

(b) FrFT and S-Method improved tomographic image with $SNR = 0$dB

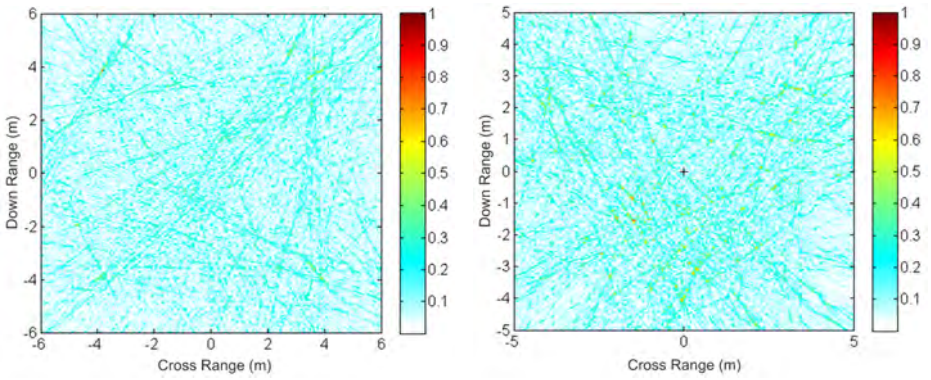

(c) FrFT and S-Method improved tomographic image with $SNR = -4$dB

(d) FrFT and S-Method improved tomographic image with $SNR = -6$dB

Figure 18: *Processed tomographic images of the four scatterer orientation for three noise levels.*

Figure 19 shows a 3D view of the tomographic image using the smear-free projections of aircraft A. The image shows the peaks of the four rotor blades tips, but with low resolution. However, Figure 20 is the same view of the same aircraft with FrFT and S-Method processing using smeared projections. This figure clearly shows four peaks corresponding to the four blade tip scatterers. The level of noise on the signal is low enough for the chirp search and extraction algorithm to function properly and hence gives a reasonably good tomographic image.

Similarly, Figure 21 shows a 3D view of the tomographic image using smear-free projections of aircraft B. Again, the low resolution and noise level gives a less defined tomographic image. The processed smeared projections using the FrFT and S-Method algorithm, for the same dataset, exaggerates the two blade tip scatterers, as shown in Figure 22. Although the image is less defined when compared with the examples in Section 6.1, the tip scatterers can be easily seen and the existence of two blade tips can be verified.

Table 2: *Radar and helicopter specific parameters of real data used to test the FrFT and S-Method algorithm.*

	Aircraft ID	
Parameters	A	B
Pulse Repetition Freq., PRF	16.7 kHz	28.9 kHz
Carrier Frequency, f_c	5.5 GHz	9.7 GHz
Rotation Rate, ω	230 RPM	350 RPM
Number of Blades	4	2
Overlapping Factor, F	0.8	0.8

The FrFT and S-Method algorithm has proven to perform well on real helicopter data with the tip scatterers easily recognisable in the tomographic image. In less noisy data and with an improvement of chirp search and extraction algorithms, the FrFT and S-Method technique could prove useful for imaging helicopter rotor blades and other rotating objects.

7 Conclusion

We have presented a new method of improving the resolution of a tomographic image of a rotating object by effectively increasing coherent integration time and using recently developed signal processing techniques.

The imaging approach is Doppler radar tomography, with the Doppler-processed cross-range profiles as projections in the tomographic processing. We have briefly reviewed the basics of this processing technique and determined its performance limit, in the case when only the Fourier transform is employed. The recently developed techniques are the fractional Fourier transform and the S-Method, here for the first time, applied to Doppler radar tomography. The usefulness of these techniques lie in their ability to identify and spectrally compress chirped signals which result from scattering centers of a rotating object. The projections are 'cleaner' and sharper, resulting in tomographic images with better resolution.

Separately, the role of the fractional Fourier transform is to identify the different chirp signals present in a CPI, based on the property that, at a particular value of the order of the transform, only those chirps with chirp rates matching the transform order can be 'de-chirped'. An extraction algorithm is then used to separate them from the other chirps in the signal. The role of the S-Method is to spectrally compress the extracted chirps in the classic frequency domain, without the undesirable effects of cross terms.

We have demonstrated the performance of this new method on a variety of rotating point scatterer examples, in varying orientations, in terms of improved resolution and in the presence of noise. We have also demonstrated the applicability of this method on real helicopter data. Despite the fact the current form of the method is not yet optimised for the complexity of blade flashes from helicopter rotor blades, the result is very promising, with the improved tomographic images showing focused blade tips, compared to smeared images generated using Fourier transform based techniques.

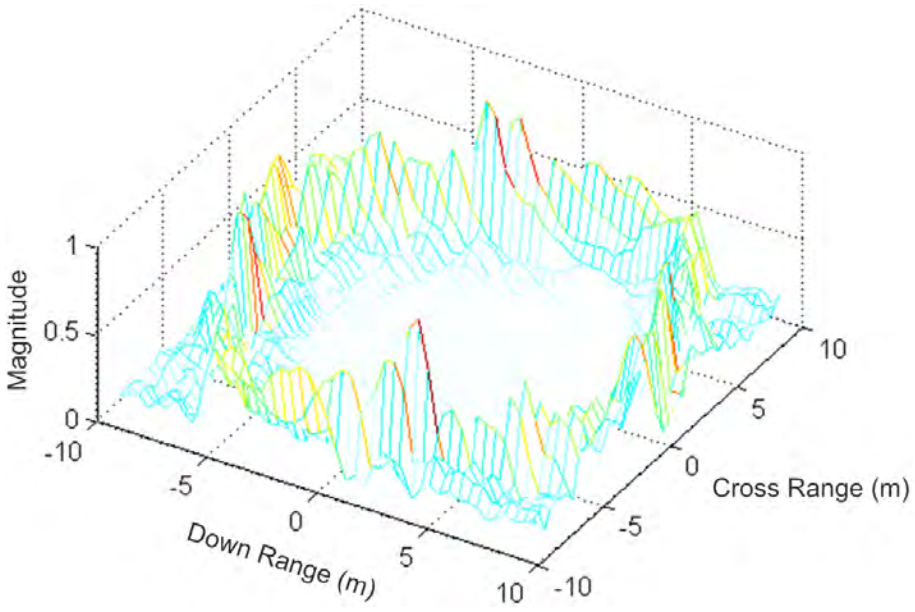

Figure 19: *3D smear-free tomographic image of aircraft A.*

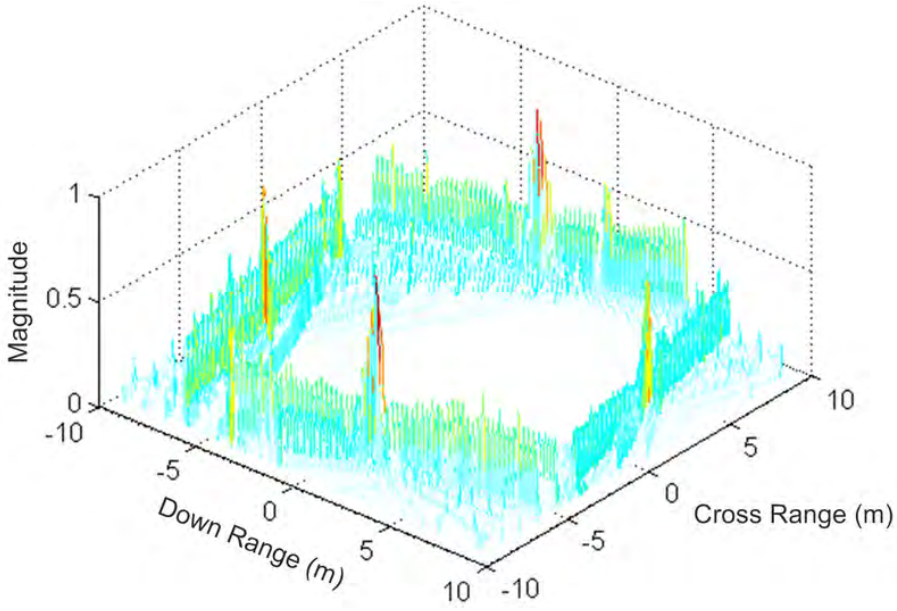

Figure 20: *3D FrFT and S-Method processed tomographic image of aircraft A.*

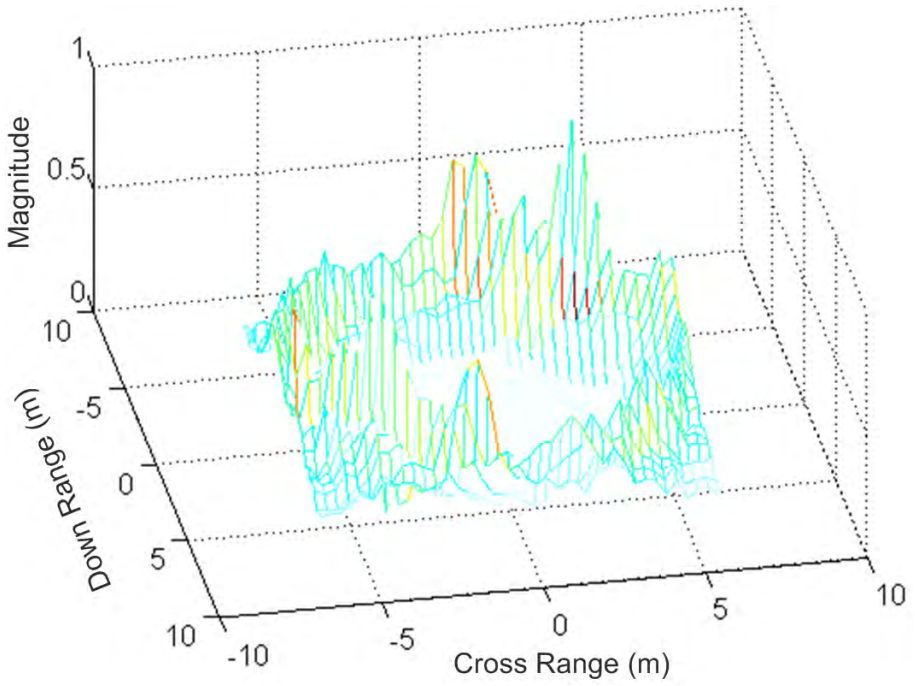

Figure 21: *3D smear-free tomographic image of aircraft B.*

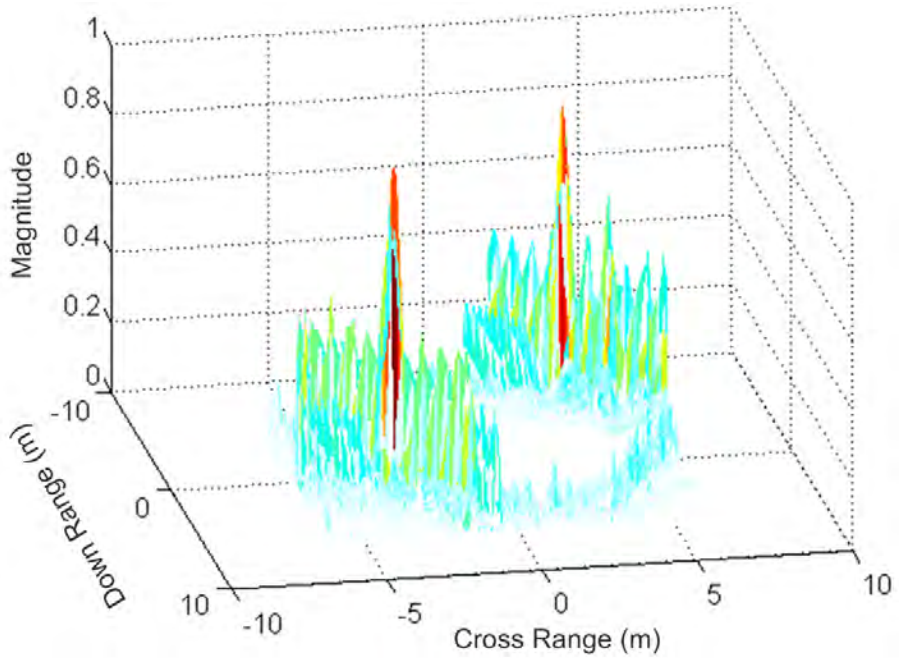

Figure 22: *3D FrFT and S-Method processed tomographic image of aircraft B.*

Other potential applications include the imaging of helicopter tail rotor blades, propellers on propeller driven aircraft, and slower rotating objects such as rotating antenna structures on ships. Work is currently underway to maximise the robustness of the proposed algorithm for many real objects of interest.

Acknowledgements

The authors would like to thank Dr. Andrew Shaw (RLMR) for his critical review comments and Dr. Desmond Yau of the Microwave Radar Branch, EWRD, DSTO Edinburgh, for his reviewing and assisting in this work and Dr. Leigh Powis (Head, AAR group) for his support.

References

1. Radon, J., *"On the determination of functions from their integral values along certain manifolds"*, translated by P.C. Parks from original German text, IEEE Transactions on Medical Imaging, Vol MI5, No.4, December 1986.

2. Kak, A., Slaney, M., *"Principles of Computerised Tomographic Imaging"*, IEEE Press, 1987.

3. Mensa, D.L., *"Coherent Doppler Tomography for Microwave Imaging"*, IEEE Transaction, Vol. 71, No. 2, June 1983.

4. Fliss, F., *"Tomographic Radar Imaging of Rotating Structures"*, SPIE, Vol. 1630, 1992.

5. Chen, V., Ling, H., *"Time-frequency Transforms for Radar Imaging and Signal Analysis"*, Artech House, 2003.

6. Thayaparan,T., *"Target Detection and Feature Extraction in Indoor and Outdoor Environments using Micro-Doppler Analysis"*, DRDC Technical Report, TM 2008-255, December 2008.

7. Scudder, H.J., *"Introduction to Computer Aided Tomography"*, IEEE Transaction, Vol. 66, June 1978.

8. Qu, Z.,*"The Convolution Back Projection Algorithm Based on Windows Function"*, IEEE Transaction, 2005.

9. Hermann, G.T., *"Image Reconstruction From Projections: Fundamentals of Computerized Tomography"*, Academic Press, 1980.

10. Natterer, F., *"Mathematics of Computerized Tomography"*, John Wiley and Son, 1986.

11. Capus, C., *"The Analysis of Multiple Linear Chirp Signals"*, IEE Transaction, 2000.

12. Ozaktas, H.M., *"Digital Computation of the Fractional Fourier Transform"*, IEEE Transaction on Signal Processing, Vol. 44, 1996.

13. Almeida, L., *"The Fractional Fourier Transform and Time-frequency Representations"*, IEEE Transactions on Signal Processing, Vol. 42, No. 11, November 1994.

14. Candan, C., *"The Discrete Fractional Fourier Transform"*, IEEE Transactions on Signal Processing, Vol. 48, No. 5, May 2000.

15. Capus, C., *"Short-time Fractional Fourier Methods for the Time-frequency Representation of Chirp Signals"*, Journal of Acoustical Society of America, Vol. 113, No. 6, June 2003.

16. Jouny, I., *"Target Identification Using Fractional Fourier Features"*, SPIE, Vol. 5426, pp.219-26 2004.

17. Tao, R., *"Short-time Fractional Fourier Transform and Its Application"*, IEEE Transactions, Vol. 58, No. 5, May 2010.

18. Zayed, A., *"On the Relationship Between the Fourier and Fractional Transforms"*, IEEE Signal Processing Letters, Vol. 3, No. 12, December 1996.

19. Stankovic, L., *"Adaptive S-Method for SAR/ISAR Imaging"*, EURASIP Journal on Advances in Signal Processing, Vol. 2008, Article ID 593216, November 2007.

20. Namias, V., *"The fractional Fourier transform and its application to quantum mechanics"*, J. Inst. Math. Appl., Vol.25, pp.241-65, 1980.

21. Liu, H. and Zhu, M. , *"Applying Fractional Fourier Transform to Radar Imaging of Moving Targets"*, 2003 IEEE International Geoscience and Remote Sensing Symposium, 2003. IGARSS '03. Proceedings, pp.4071-73, Vol.6, 2003.

22. Ai-fang, L., Lin, J. and Zhong, L., *"Application of Fractional Fourier Transform to ISAR Imaging of Maneuvering Targets"*, Proc. of SPIE Vol.6043, 2005.

23. Cao, M., Fu, Y., Jiang, W., Li, X., Zhuang, Z., *"High Resolution Range Profile Imaging of High Speed Moving Targets Based on Fractional Fourier Transform"*, Proc. of SPIE Vol.6786, 2007.

24. Huang, J-B., Rao, R., and Wang, Y., *"Fractional Fourier Transform and its Application to SAR Imaging of Moving Targets"*, 2nd Asian-Pacific Conference on Synthetic Aperture Radar, APSAR 2009, pp.709-12, 2009.

DEFENCE SCIENCE AND TECHNOLOGY ORGANISATION DOCUMENT CONTROL DATA	1. CAVEAT/PRIVACY MARKING

2. TITLE	3. SECURITY CLASSIFICATION
Application of the Fractional Fourier Transform and S-Method in Doppler Radar Tomography	Document (U) Title (U) Abstract (U)
4. AUTHORS	5. CORPORATE AUTHOR
H.T. Tran and R. Melino	Defence Science and Technology Organisation PO Box 1500 Edinburgh, South Australia 5111, Australia

6a. DSTO NUMBER	6b. AR NUMBER	6c. TYPE OF REPORT	7. DOCUMENT DATE
DSTO–RR–0357	014–825	Research Report	August, 2010

8. FILE NUMBER	9. TASK NUMBER	10. SPONSOR	11. No. OF PAGES	12. No. OF REFS
2010/1081590/1	07/213		34	24

13. URL OF ELECTRONIC VERSION	14. RELEASE AUTHORITY
http://www.dsto.defence.gov.au/corporate/reports/DSTO–RR–0357.pdf	Chief, Electronic Warfare and Radar Division

15. SECONDARY RELEASE STATEMENT OF THIS DOCUMENT

Approved for Public Release

OVERSEAS ENQUIRIES OUTSIDE STATED LIMITATIONS SHOULD BE REFERRED THROUGH DOCUMENT EXCHANGE, PO BOX 1500, EDINBURGH, SOUTH AUSTRALIA 5111

16. DELIBERATE ANNOUNCEMENT

No Limitations

17. CITATION IN OTHER DOCUMENTS

No Limitations

18. DSTO RESEARCH LIBRARY THESAURUS

Fractional Fourier transform,
S-Method
Tomography
Linear FM signals
Time-frequency transform.

19. ABSTRACT

Doppler radar tomography is a technique which uses only the Doppler profiles of a rotating target as projections in two-dimensional radar tomography to obtain an image of the target. The work demonstrates, for the first time, the application of the fractional Fourier transform and the S-Method in improving the image resolution. The performance is shown to be significantly better than that available with traditional Fourier transform-based methods.